Microglia Dysfunction Caused by the Loss of Rhoa Disrupts Neuronal Physiology and Leads to Neurodegeneration
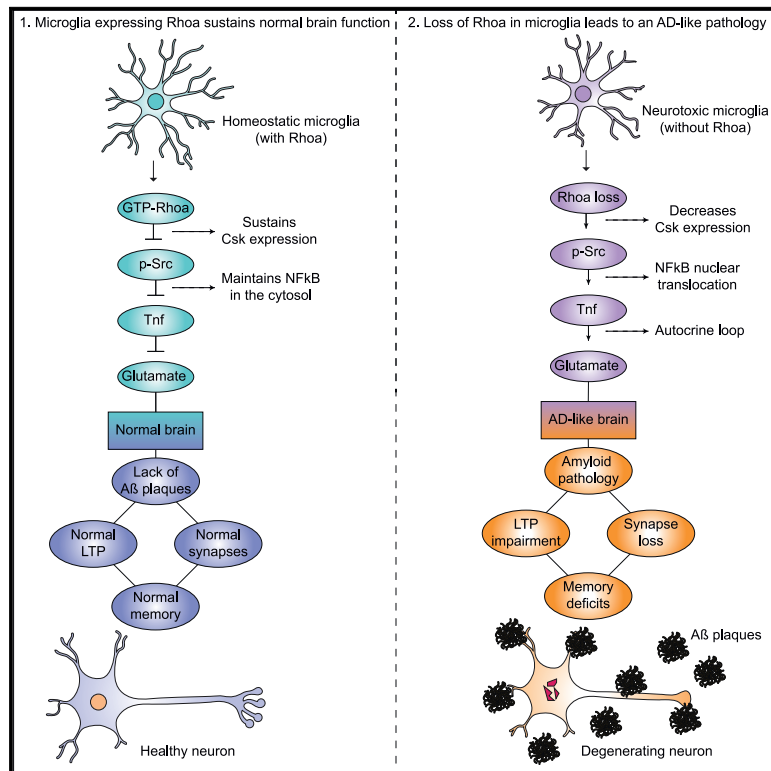
Graphical Abstract

1. Microglia expressing Rhoa sustains normal brain function
2. Loss of Rhoa in microglia leads to an AD-like pathology

Authors

Renato Socodato, Camila C. Portugal, Teresa Canedo, ..., Teresa Summavielle, António F. Ambrosio, João B. Relvas

Correspondence

jrelvas@ibmc.up.pt

In Brief

Socodato et al. show that ablating Rhoa in microglia of young adult mice is sufficient to produce major hallmarks of AD (including amyloid pathology, impairment of long-term synaptic plasticity, synapse loss, and memory deficits), suggesting that disrupting Rho GTPase signaling in microglia might underlie the neurodegenerative process in AD.

Highlights

- Microglia lacking Rhoa become neurotoxic

- Rhoa ablation in microglia leads to amyloidosis, synapse loss, and memory deficits

- Rhoa ablation in microglia is sufficient to produce an AD-like pathology

- Rhoa activation is decreased in microglia from AD mice

CellPress

Article

Microglia Dysfunction Caused by the Loss of Rhoa Disrupts Neuronal Physiology and Leads to Neurodegeneration

Renato Socodato,[1,14] Camila C. Portugal,[1,14] Teresa Canedo,[1] Artur Rodrigues,[1] Tiago O. Almeida,[1] Joana F. Henriques,[1] Sandra H. Vaz,[12,13] João Magalhães,[1] Cátia M. Silva,[1] Filipa I. Baptista,[5,6,8] Renata L. Alves,[1] Vanessa Coelho-Santos,[7] Ana Paula Silva,[7] Roberto Paes-de-Carvalho,[10] Ana Magalhães,[1] Cord Brakebusch,[11] Ana M. Sebastião,[12,13] Teresa Summavielle,[1,3] António F. Ambrosio,[5,6,8,9] and João B. Relvas[1,2,4,15,*]

[1]Instituto de Investigacao e Inovacao em Saude and Instituto de Biologia Molecular e Celular, Porto, Portugal
[2]Faculdade de Medicina, Universidade do Porto, Porto, Portugal
[3]Escola Superior de Saúde, Politécnico do Porto, Porto, Portugal
[4]The Discoveries Centre for Regeneration and Precision Medicine, Porto Campus, Porto, Portugal
[5]Coimbra Institute for Clinical and Biomedical Research (iCBR), Coimbra, Portugal
[6]Center for Innovative Biomedicine and Biotechnology (CIBB), Faculty of Medicine, Coimbra, Portugal
[7]Institute of Pharmacology and Experimental Therapeutics, Faculty of Medicine, University of Coimbra, Coimbra, Portugal
[8]Clinical Academic Center of Coimbra (CACC), Coimbra, Portugal
[9]Association for Innovation and Biomedical Research on Light and Image (AIBILI), Coimbra, Portugal
[10]Department of Neurobiology and Program of Neurosciences, Institute of Biology, Fluminense Federal University, Niteroi, Brazil
[11]Molecular Pathology Section, BRIC, Københavns Biocenter, Copenhagen, Denmark
[12]Instituto de Farmacologia e Neurociências, Lisboa, Portugal
[13]Instituto de Medicina Molecular, Faculdade de Medicina, Universidade de Lisboa, Lisboa, Portugal
[14]These authors contributed equally
[15]Lead Contact
*Correspondence: jrelvas@ibmc.up.pt
https://doi.org/10.1016/j.celrep.2020.107796

SUMMARY

Nervous tissue homeostasis requires the regulation of microglia activity. Using conditional gene targeting in mice, we demonstrate that genetic ablation of the small GTPase Rhoa in adult microglia is sufficient to trigger spontaneous microglia activation, producing a neurological phenotype (including synapse and neuron loss, impairment of long-term potentiation [LTP], formation of β-amyloid plaques, and memory deficits). Mechanistically, loss of Rhoa in microglia triggers Src activation and Src-mediated tumor necrosis factor (TNF) production, leading to excitotoxic glutamate secretion. Inhibiting Src in microglia Rhoa-deficient mice attenuates microglia dysregulation and the ensuing neurological phenotype. We also find that the Rhoa/Src signaling pathway is disrupted in microglia of the APP/PS1 mouse model of Alzheimer disease and that low doses of Aβ oligomers trigger microglia neurotoxic polarization through the disruption of Rhoa-to-Src signaling. Overall, our results indicate that disturbing Rho GTPase signaling in microglia can directly cause neurodegeneration.

INTRODUCTION

Microglia are yolk-sack-derived myeloid cells that populate the early-developing nervous system (Ginhoux et al., 2010; Kierdorf et al., 2013; Schulz et al., 2012). Under physiological conditions, microglia continuously extend and retract their cellular processes, monitoring the central nervous system (CNS) parenchyma for tissue damage or infections and checking the functional status of brain synapses (Crotti and Ransohoff, 2016). Although attempts are made to repair injuries to the parenchyma, exacerbation or prolonged microglial activation may trigger and/ or accelerate neuronal damage in neurogenerative conditions or delay CNS recovery after insults (Gómez-Nicola et al., 2013, Rice

et al., 2015; Spangenberg et al., 2016). Such a detrimental role for microglia can be attributed to the loss/disruption of microglia immune restrain mechanisms (Deczkowska et al., 2018), which leads to sustained deregulation of their activation and consequent overproduction of proinflammatory cytokines (interleukin-1β [IL-1β] and tumor necrosis factor [TNF]), nitric oxide (NO), and reactive oxygen species (ROS) and an increased release of glutamate (Block et al., 2007).

Proinflammatory microglial activation is associated with profound changes in microglia morphology requiring cytoskeleton reorganization (abd-el-Basset and Fedoroff, 1995; Kaur, 1997). The GTPases of the Rho family, from which Rhoa, Rac1, and Cdc42 are the founding members, are key orchestrators of
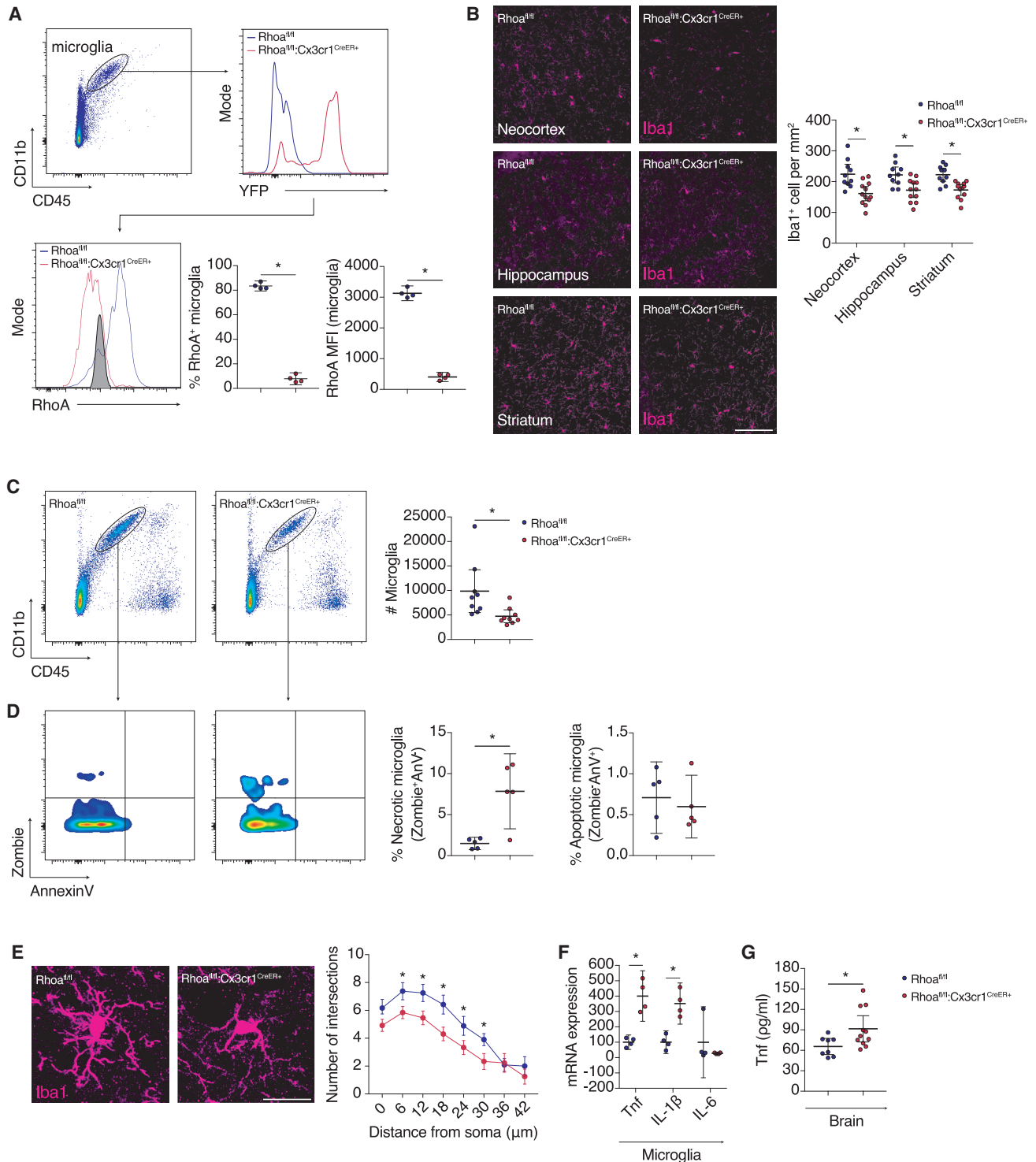
Figure 1. Rhoa Is Required for Microglia Survival, and Its Ablation Triggers Spontaneous Microglia Activation

(A) Expression of Rhoa in microglia from the brains of Rhoa^{fl/fl} and Rhoa^{fl/fl}:Cx3cr1[CreER+] mice 35–45 days post-TAM (n = 4 mice).

(B) Confocal images for Iba1 on tissue sections for the indicated brain regions from Rhoa^{fl/fl} and Rhoa^{fl/fl}:Cx3cr1[CreER+] 35–45 days post-TAM (n = 10–12 mice). Scale bars: 50 μm.

(C) Flow cytometry analysis of microglial numbers in Rhoa^{fl/fl} and Rhoa^{fl/fl}:Cx3cr1[CreER+] mice 35–45 days post-TAM (n = 9 mice).

(D), Flow cytometry analysis of cell death markers in microglia from Rhoa^{fl/fl} and Rhoa^{fl/fl}:Cx3cr1[CreER+] mice 150 days post-TAM (n = 5 mice per condition).

(E) Sholl analysis in microglia from the neocortex of Rhoa^{fl/fl} and Rhoa^{fl/fl}:Cx3cr1[CreER+] 35–45 days post-TAM (n = 12–13 cells from 3 mice). Scale bar: 20 μm.

(legend continued on next page)

cytoskeleton dynamics (Bustelo et al., 2007) and are therefore well positioned to govern microglia activation. Typical GTPases function as binary switches by cycling between a GDP-bound inactive, "off" state, and a GTP-bound active, "on" state, in which they can directly interact with downstream effectors to regulate different cell functions (Hodge and Ridley, 2016). Rho GTPases play important roles during CNS development, and dysregulation of their expression and/or activity is associated with different neurological disorders (Stankiewicz and Linseman, 2014). Indeed, changes in Rhoa activity or in the activities of its effectors are implicated in several neurodegenerative conditions, including stroke, Alzheimer disease (AD) and Parkinson disease, and amyotrophic lateral sclerosis (DeGeer and Lamarche-Vane, 2013; Droppelmann et al., 2014). Here, using tamoxifen (TAM)-inducible conditional gene inactivation in mice, we investigated the bona fide function of Rhoa in microglia. Our data reveal critical roles for Rhoa signaling in regulating microglia immune activity and microglia-dependent synaptic integrity.

RESULTS

Conditional Ablation of Rhoa in Adult Microglia

To study the role of Rhoa in adult microglia, we crossed Cx3cr1[CreER-IRES-EYFP] mice (Parkhurst et al., 2013; Goldmann et al., 2013; Yona et al., 2013) with mice carrying Rhoa conditional alleles (Herzog et al., 2011; Jackson et al., 2011; Figure S1A). In Cx3cr1[CreER] mice, the CreER-IRES-EYFP transgene is transcriptionally active in Iba1^{+} brain myeloid cells (Goldmann et al., 2016; Figure S1B) and microglia (Figure S1C). As expected, following TAM administration, Cre-mediated recombination substantially decreased Rhoa expression in Rhoa^{fl/fl}:Cx3cr1[CreER+] microglia (Figures 1A and S1D). Because Rhoa^{fl/fl}:Cx3cr1[CreER+] mice have only one intact copy of Cx3cr1 and decreased Cx3cr1 protein levels could per se disrupt microglia homeostasis and be a confounding factor affecting the conclusions of our study, we confirmed that the number of microglia expressing Cx3cr1 as well as microglial number did not vary significantly between Rhoa^{fl/fl} and Cx3cr1[CreER+] (Figure S1E). We also included other controls to further validate our experimental set up (Figures S1F–S1H).

Rhoa Is Required for Microglial Survival and Activation

We then evaluated the requirement of Rhoa for microglia homeostasis. We observed a decrease in the number of Iba1^{+} cells in the neocortex, hippocampus, and striatum comparing Rhoa^{fl/fl} with Rhoa^{fl/fl}:Cx3cr1[CreER+] littermates (Figure 1B). Using flow cytometry, we confirmed a decrease in the numbers of microglia in Rhoa^{fl/fl}:Cx3cr1[CreER+] brains (Figure 1C). Such a decrease in microglial numbers persisted in the brains of mature adult Rhoa^{fl/fl}:Cx3cr1[CreER+] mice (Figure S2A). The decrease on microglial numbers following Rhoa ablation could be caused by

increased microglial cell death. Indeed, we found increased necrosis (Zombie[+]Anv[−]) in Rhoa^{fl/fl}:Cx3cr1[CreER+] microglia (Figure 1D). However, microglial numbers in Rhoa^{fl/fl}:Cx3cr1[CreER+] mice 40 days post-TAM (Figure 1C) and 150 days post-TAM (Figure S2A) were comparable. This suggested that proliferation could be counterbalancing cell death to stabilize microglial numbers. Accordingly, we found increased microglial proliferation in mature Rhoa^{fl/fl}:Cx3cr1[CreER+] mice compared with Rhoa^{fl/fl} littermates (Figure S2B).

Changes in microglial cell morphology are usually concurrent with alterations in microglial function. Morphological analysis revealed that Rhoa mutant microglia were less ramified than Rhoa^{fl/fl} microglia (Figures 1E and S2C). Modifications in actin cytoskeleton organization and dynamics most likely underlie the changes found in microglia morphology. Inhibiting Rhoa activation in microglial cultures by expressing a dominant-negative Rhoa mutant (Rhoa[T19N]; Figure S2D), resulted in a loss of actin stress fibers (Figure S2E) and decreased the speed of microglia protrusion extension, which is regulated by actin dynamics (Figure S2F).

Next, we evaluated whether the production of inflammatory cytokines was increased in Rhoa^{fl/fl}:Cx3cr1[CreER+] microglia. Indeed, Rhoa mutant microglia contained greater amounts of mRNA transcripts coding for the classical proinflammatory cytokines TNF and IL-1β, but not for IL-6 (Figure 1F). The increased production of TNF in Rhoa mutant microglia resulted in increased TNF amounts in Rhoa^{fl/fl}:Cx3cr1[CreER+] brains (Figure 1G).

In addition to microglia, long-lived nonparenchymal macrophages residing on brain interfaces are potentially targeted in Cx3cr1[CreER+] mice (Goldmann et al., 2016). However, and in contrast to microglia, Rhoa expression in brain macrophages (CD11b^{+}CD45^{high} cells; gated as shown in Figure S2G) as well as their numbers, viability, and reactivity were comparable between Rhoa^{fl/fl}:Cx3cr1[CreER+] mice and aged-matched Rhoa^{fl/fl} littermates (Figures S2G and S2H). Because Cx3cr1 is also expressed on peripheral organs (Jung et al., 2000), some degree of Cre-mediated recombination was expected to occur outside the CNS of Rhoa^{fl/fl}:Cx3cr1[CreER+] mice (Parkhurst et al., 2013). However, blood monocytes and spleen macrophages (Figure S2I) showed a similar abundance of Rhoa mRNA transcripts between Rhoa^{fl/fl}:Cx3cr1[CreER+] mice and Rhoa^{fl/fl} littermates (Figure S2J). The percentage of different CD45^{+} myeloid populations was also comparable between the genotypes (Figures S2K and S2L), indicating that the Rhoa mutant phenotype relates predominantly to microglia and not to macrophages.

To further establish that the loss of Rhoa in microglia would be sufficient to trigger their activation spontaneously in a cell autonomous manner, we depleted Rhoa in different cell culture experimental setups and evaluated microglia activation. We found that (1) loss of Rhoa in primary cortical microglial cultures obtained from Rhoa floxed mice (Figure S3A) led to an increased

---

(F) qRT-PCR in microglia sorted from brains of Rhoa^{fl/fl} and Rhoa^{fl/fl}:Cx3cr1[CreER+] mice 35–45 days post-TAM (n = 4 mice).

(G) TNF amounts (ELISA) in Rhoa^{fl/fl} and Rhoa^{fl/fl}:Cx3cr1[CreER+] brains 35–45 days post-TAM (n = 8–11 mice).

Data are represented as mean with 95% confidence interval (CI). *p < 0.05 (Mann-Whitney test in A, C, D, F, and G; 2-way ANOVA in B and E). See also Figures S1–S3.
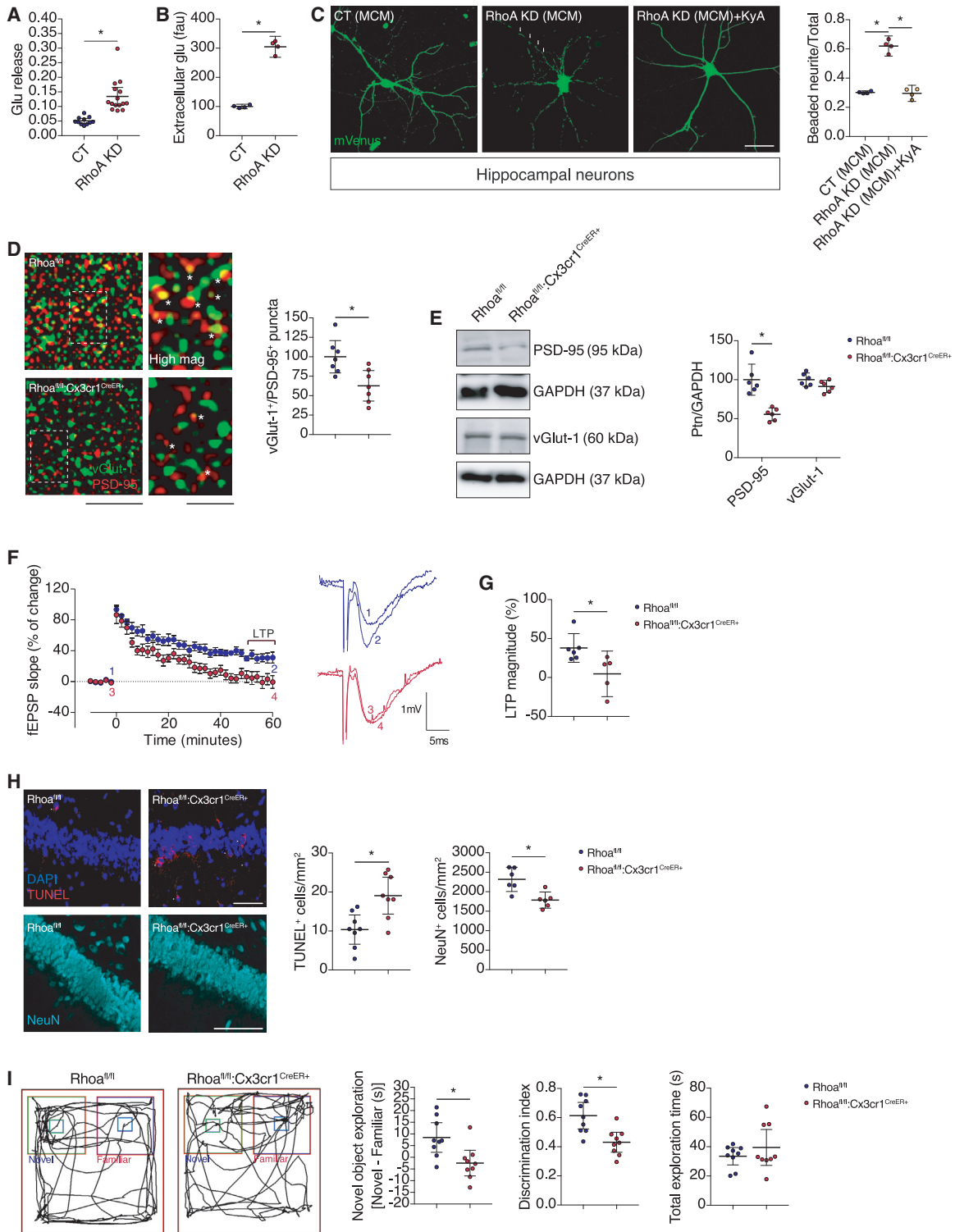
Figure 2. Rhoa Deficiency in Adult Microglia Leads to Phenotypic Features Underlying Neurological Disorders

(A) Primary cortical microglial cultures expressing FLIPE[600nSurface] were transduced with lentiviruses coding pLKO or Rhoa shRNA (CT; n = 11–15 cells from 3 cultures).

(B) Extracellular glutamate in the culture media of pLKO and Rhoa KD primary cortical microglia cultures (n = 4 cultures). faus, fluorescence arbitrary units.

expression and secretion of TNF (Figures S3B and S3C), and that (2) knocking down Rhoa in microglial cell lines (Figure S3D) also increased TNF expression (Figure S3E) and secretion (Figure S3F), (3) increased nuclear factor κB (NF-κB) activation (Figures S3G and S3H), and (4) led to the degradation of the inhibitor of κB (Figure S3I; Shcherbakova et al., 2016).

Ablation of Rhoa in Microglia Leads to a Neurological Phenotype

Increased secretion of TNF by microglia can be detrimental to neurons because TNF autocrinally increases the release of glutamate (Takeuchi et al., 2006), thus causing excitotoxic damage to neurites and neurons (Maezawa and Jin, 2010). Using the glutamate release FRET biosensor FLIPE600n^{Surface}, which specifically discriminates glutamate release over its uptake or its intracellular mobilization via cell metabolism (Okumoto et al., 2005), we showed that Rhoa knockdown (KD) increased glutamate release from living primary cortical microglia (Figure 2A). This increased release led to an accumulation of glutamate in the extracellular space (Figure 2B). Incubation of primary hippocampal neurons with microglia conditioned media (MCM) collected from primary cortical microglia knocked down for Rhoa increased neurite beading (Figure 2C), a characteristic of glutamate excitotoxicity (Maezawa and Jin, 2010). Confirming that microglia-secreted glutamate was driving neurite damage, pharmacological inhibition of the NMDA-type of glutamate receptors on hippocampal neurons abrogated the neurite beading effect of Rhoa KD MCM (Figure 2C).

We then evaluated the impact of microglia-dependent neurotoxicity in Rhoa$^{fl/fl}$:Cx3cr1^{CreER+} mice. Here, we focused our analyses primarily on the hippocampus because this brain region is vulnerable to TNF-induced glutamate excitotoxicity (Yu et al., 2002). We found less excitatory synaptic puncta in Rhoa$^{fl/fl}$:Cx3cr1^{CreER+} hippocampus (evaluated by the number of vGlut-1$^+$/PDS-95$^+$ colocalization puncta) than that in Rhoa$^{fl/fl}$ littermates (Figure 2D). The amounts of vGlut-1 protein were comparable, whereas the amounts of PSD-95 were significantly reduced in the Rhoa$^{fl/fl}$:Cx3cr1^{CreER+} hippocampus (Figure 2E).

Because synapse loss can adversely affect neuronal plasticity, we assessed the long-term potentiation (LTP) of hippocampal synapses in Rhoa$^{fl/fl}$:Cx3cr1^{CreER+} animals. A θ-burst stimulation of hippocampal slices from Rhoa$^{fl/fl}$ mice led to an initial enhancement of field excitatory post-synaptic potential (fEPSP) slope followed by a decrease and stabilization period, but at the end of recording period, fEPSP slope values remained higher than before the θ-burst stimulation (Figure 2F, blue circles). In Rhoa$^{fl/fl}$:Cx3cr1^{CreER+} slices, however, the same θ-burst stimulation caused only an initial transient increase in fEPSP slope values (Figure 2F, red circles), which decreased progressively toward pre-θ-burst levels. LTP magnitude was significantly lower on hippocampal slices from Rhoa$^{fl/fl}$:Cx3cr1^{CreER+} mice (Figure 2G), indicating a marked LTP impairment.

Changes in synapse number/function may be associated with neuronal cell death (Palop et al., 2006). Indeed, we found an increase in TUNEL$^+$ cells in the Rhoa$^{fl/fl}$:Cx3cr1^{CreER+} hippocampus (Figure 2H), indicating neuronal apoptosis. In line with this, Rhoa$^{fl/fl}$:Cx3cr1^{CreER+} hippocampi contained less NeuN-positive neurons than hippocampi from Rhoa$^{fl/fl}$ littermates (Figure 2H).

Synapse loss and LTP impairment can result in behavioral deficits. To address this possibility, we compared the performance of Rhoa$^{fl/fl}$:Cx3cr1^{CreER+} and Rhoa$^{fl/fl}$ mice in different behavioral paradigms, including elevated plus-maze (EPM) to evaluate anxiety-like behavior, open field (OF) to test general activity levels and gross motor function, and novel object recognition (NOR) to test recognition memory. Both EPM (Figure S3J) and OF (Figures S3K–S3P) tests did not show significant differences between genotypes. In the NOR test, however, Rhoa$^{fl/fl}$:Cx3cr1^{CreER+} mice spent less time exploring the novel object (Figure 2I) and their capacity to discriminate the novel object over the familiar object was reduced, indicating deficits in recognition memory (Figure 2I).

Given that Rhoa, Rhob, and Rhoc share high degree of similarity (Wheeler and Ridley, 2004), we asked whether depleting Rhob or Rhoc would also lead to spontaneous microglial activation. Contrasting to Rhoa KD, the KD of Rhob or Rhoc (validations in Figure S4A) did not alter microglia morphology (Figure S4B), ROS production (Figure S4C), glutamate release (Figure S4D), NF-κB nuclear translocation (Figure S4E), or TNF release (Figure S4F). Furthermore, CM from Rhob KD or Rhoc KD microglial cultures did not induce neurite beading on hippocampal neurons (Figure S4G). To check whether a compensatory Rhoc upregulation

(C) Primary hippocampal neuronal cultures expressing mVenus were incubated for 24 h with conditioned media from primary microglial cultures (MCM) obtained from WT mice that were previously infected with pLKO or Rhoa shRNA lentiviruses (n = 3–4 cultures). Under some conditions, neurons were co-incubated with the NMDA receptor antagonist kynurenic acid (KyA; 1 μM). Arrowheads display a beaded neurite. Scale bar: 50 μm.

(D) vGlut-1 (green) and PSD-95 (red) immunolabeling on hippocampus CA1 region of Rhoa$^{fl/fl}$ and Rhoa$^{fl/fl}$:Cx3cr1^{CreER+} mice 35–45 days post-TAM (n = 7 mice). Scale bars: 5 μm and 1 μm (high mag). White asterisks denote synaptic puncta.

(E) Western blot for PSD-95 and vGlut-1 on brains lysates from Rhoa$^{fl/fl}$ and Rhoa$^{fl/fl}$:Cx3cr1^{CreER+} mice 35–45 days post-TAM (n = 6 mice). GAPDH was the loading control.

(F and G) The averaged time course changes in field excitatory post-synaptic potential (fEPSP) slope induced by θ-burst stimulation in Rhoa$^{fl/fl}$ (n = 11 slices from 6 mice) and Rhoa$^{fl/fl}$:Cx3cr1^{CreER+} (n = 9 slices from 5 mice) 35–45 days post-TAM (F). Ordinates represent normalized fEPSP slopes, from which 0% corresponds to slopes averaged and recorded for 10 min before θ-burst stimulation ([−0.99 ± 0.04 mV/ms (Rhoa$^{fl/fl}$], −0.93 ± 0.04 mV/ms [Rhoa$^{fl/fl}$:Cx3cr1^{CreER+}]), and the abscissa represents the time that average begun. Experiments are the average of six consecutive responses obtained for Rhoa$^{fl/fl}$ or Rhoa$^{fl/fl}$:Cx3cr1^{CreER+} mice before (1 or 3) and 58–60 min after (2 or 4) θ-burst stimulation and is composed by the stimulus artifact, followed by the pre-synaptic fiber volley and the fEPSP. (G) The magnitude of LTP obtained in slices from each genotype; the values in ordinates represent the average of the fEPSP recorded 50–60 min after LTP induction, normalized to pre θ-burst values.

(H) Confocal images of hippocampi from Rhoa$^{fl/fl}$ and Rhoa$^{fl/fl}$:Cx3cr1^{CreER+} 35–45 days post-TAM (n = 8 mice for TUNEL; n = 6 mice for NeuN). Scale bars: 100 μm.

(I) Rhoa$^{fl/fl}$ and Rhoa$^{fl/fl}$:Cx3cr1^{CreER+} were evaluated in the NOR test (after a 4-h delay) 35–45 days post-TAM (n = 9 mice).

Data are represented as mean with 95% CI. *p < 0.05 (Mann-Whitney test in A, B, and D–I; Kruskal-Wallis test in C). See also Figures S3 and S4.
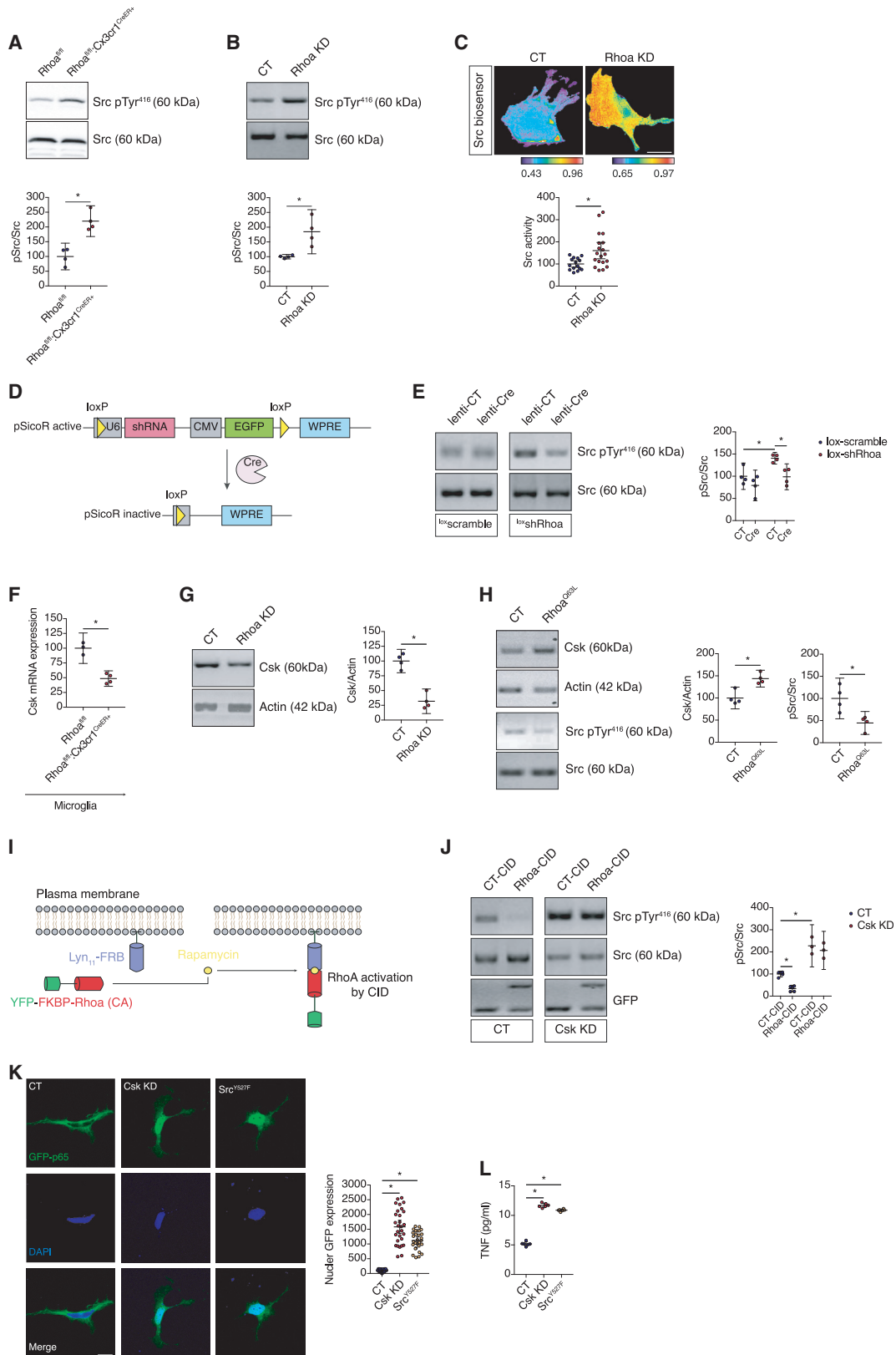
(legend on next page)

could explain the microglia activation triggered by Rhoa KD, we measured Rhoc activity in living Rhoa KD microglia and detected no overt difference in basal Rhoc activation (Figure S4H).

Rhoa Restrains Src Tyrosine Kinase Activity in Microglia

We next investigated the signaling pathway downstream of Rhoa controlling microglial activation. Csk, the endogenous repressor of Src family of tyrosine kinases (Nada et al., 1991), plays key roles in inflammation (Thomas et al., 2004). Besides, Src, the prototype and founding SFK (Src family kinase) member, is a key regulator of microglia activation (Socodato et al., 2015b). Therefore, Csk/Src emerged as good candidates for controlling microglial function, and we hypothesized that Rhoa might modulate microglia activation by this pathway.

To test this hypothesis, we investigated whether Rhoa deficiency increased Src activity in microglia. Rhoa$^{fl/fl}$:Cx3cr1^{CreER+} microglia contained greater amounts of active Src than control microglia (Figure 3A). Src activity was also increased in Rhoa KD N9 microglia and in Rhoa KD CHME3 microglia (Figures 3B and 3C). To further demonstrate that Src activity is directly linked to Rhoa function, we used the pSicoR vector (Ventura et al., 2004). In the pSicoR vector system, Cre expression causes recombination and excision of both short hairpin RNA (shRNA) and EGFP sequences, turning their expression off (Figure 3D). We found that activation of Src did not change by expressing a scrambled shRNA sequence in lenti-CT microglia or in lenti-Cre microglia (Figure 3E), but significantly increased by expressing short-hairpin Rhoa (shRhoa) sequences in lenti-CT microglia (Figure 3E). Confirming the Rhoa-dependent Src modulation, expressing shRhoa in lenti-Cre microglia excised shRhoa sequences and Src activation was retained to control levels (Figure 3E).

Csk is the endogenous repressor of Src, and we observed a decrease of Csk mRNA transcripts in Rhoa$^{fl/fl}$:Cx3cr1^{CreER+} microgl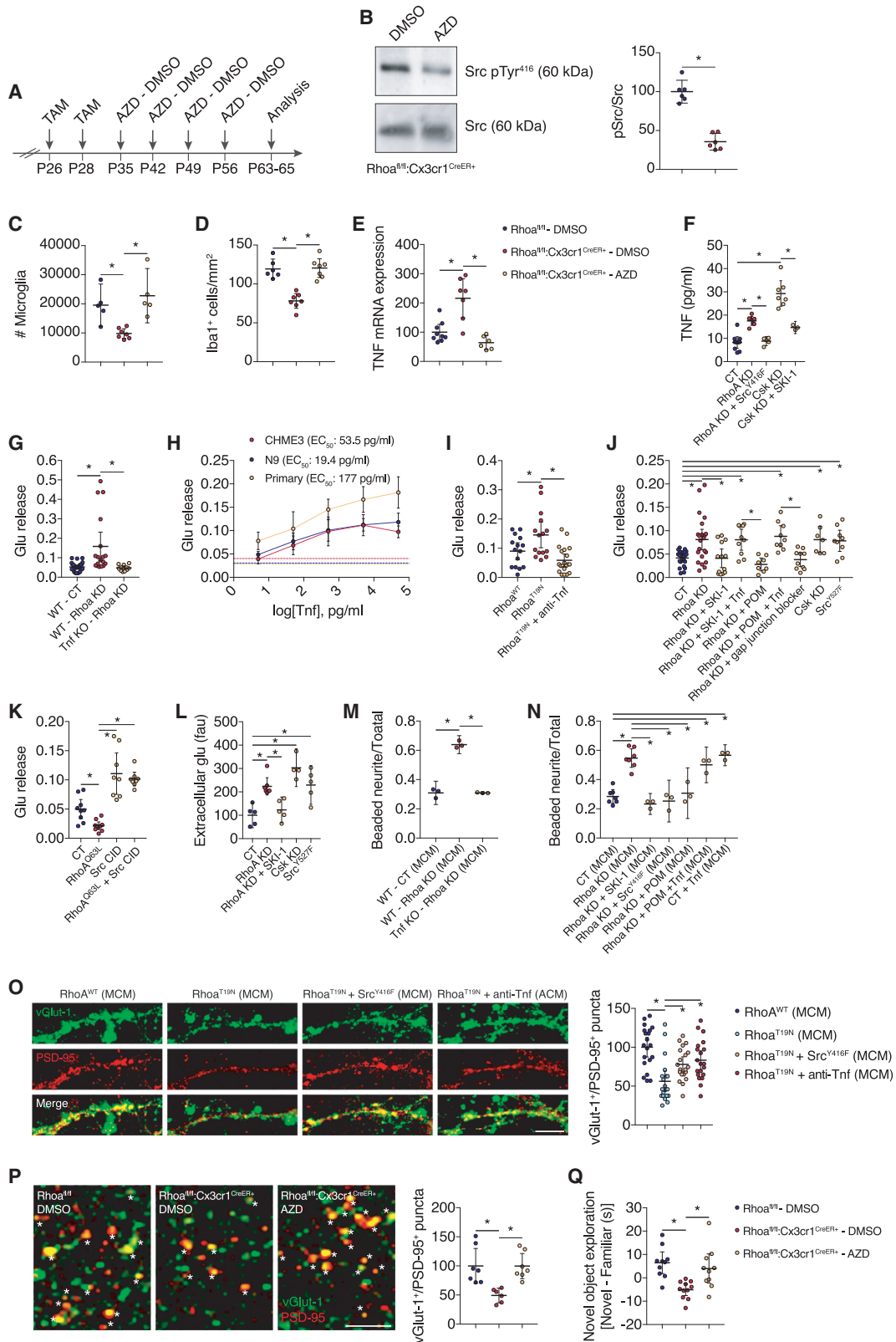ia (Figure 3F) and of Csk protein amounts in Rhoa KD N9 microglia (Figure 3G). To further link Rhoa activity with the regulation of Csk expression, we forced Rhoa activation by expressing the constitutively active Rhoa mutant Rhoa^{Q63L} in microglia. CHME3 microglia expressing Rhoa^{Q63L} had greater amounts of Csk and, consequently, lesser amounts of active Src (Figures 3H, S4I, and S4J), suggesting that Rhoa is an upstream regulator of the Csk/Src pathway in microglia.

To strengthen the link between Rhoa activity, Csk expression, and Src activity in microglia, we tested whether depleting Csk while activating Rhoa would result in Src activation. We forced Rhoa activation using a Rho GTPase chemical inducible dimerization (CID) strategy (Figure 3I; Inoue et al., 2005). In this experimental set-up, the FK506 binding protein (FKBP) and rapamycin binding domain of mTOR (FRB) is fused to the membrane-targeting sequence of Lyn (Lyn$_{11}$-FRB) to provide a plasma membrane anchor for the constitutively active form of Rhoa (Rhoa CA), which is expressed as a cytosolic fusion with FKBP and YFP. When microglia expressing both constructs are exposed to rapamycin, YFP-FKBP-Rhoa (CA) rapidly translocates to the plasma membrane and binds to Lyn$_{11}$-FRB, triggering fast activation of Rhoa (Inoue et al., 2005; Figure 3I). Indeed, following exposure to rapamycin, Src activation decreased in pLKO CHME3 microglia co-expressing Lyn$_{11}$-FRB and YFP-FKBP-Rhoa (CA) (Rhoa-CID) relative to microglia co-expressing Lyn$_{11}$-FRB and YFP-FKBP (CT-CID) (Figure 3J). However, in Csk-depleted microglia (Csk KD; validation in Figure S4K), triggering activation of Rhoa (Rhoa-CID) failed to decrease Src activation (Figure 3J).

Lastly, we examined whether forcing Csk downregulation or Src hyperactivation would be sufficient to activate microglia. Csk KD, which caused a large increase in Src activation (Figure S4L), or expressing the constitutively active Src mutant Src^{Y527F} (Figure S4L; with additional control in Figure S4M) led to NF-κB activation (Figure 3K) and increased TNF secretion (Figure 3L) in CHME3 microglia.

Figure 3. Loss of Rhoa in Adult Microglia Leads to Src Hyperactivation through Csk

(A) Western blot for Src pTyr^{416} on lysates from magnetic-activated cell sorting (MACS)-separated microglia from Rhoa$^{fl/fl}$ and Rhoa$^{fl/fl}$:Cx3cr1^{CreER+} mice 90 days post-TAM (n = 4 mice). Src was the loading control.

(B) Western blot for Src pTyr^{416} on lysates from control (CT) or Rhoa shRNA (Rhoa KD) stable N9 microglial cell sub-clones (n = 4 cultures). Src was the loading control.

(C) CHME3 microglial cultures expressing the Src FRET biosensor (KRas Src YPet) were transduced with pLKO or Rhoa shRNA lentiviruses (n = 15–19 cells from 3 cultures). Pseudocolor ramps represent min/max CFP/FRET ratios. Scale bar: 5 μm.

(D) Schematic representation of pSicoR vector-dependent knockdown of Rhoa (active pSicoR). Rhoa re-expression (inactive pSicoR) is achieved after Cre-dependent recombination of loxP sites.

(E) Western blots for Src pTyr^{416} on lysates from CHME3 microglial cells transduced with lentiviruses carrying pSicoR with a scrambled sequence (lox-scramble-lox) or Rhoa shRNA (lox-shRhoa-lox) (n = 4 cultures). Under some conditions, cells were transfected with an empty vector (lenti-CT) or with a Cre recombinase-expressing vector (lenti-Cre). Src was the loading control.

(F) qRT-PCR on sorted brain microglia from of Cx3cr1^{CreER+} and Rhoa$^{fl/fl}$:Cx3cr1^{CreER+} 35–45 days post-TAM (n = 3-4 mice).

(G) Western blot for Csk on lysates from control (CT) or Rhoa shRNA (Rhoa KD) stable N9 microglial cell sub-clones (n = 4 cultures). Actin was the loading control.

(H) Western blot for Csk or Src pTyr^{416} on lysates from CHME3 microglial cells transfected with the Rhoa^{Q63L} mutant. Actin and Src were the loading controls (n = 4 cultures).

(I) Schematic representation of Rhoa activation using chemical-inducible dimerization (CID).

(J) Western blot for Src pTyr^{416} on lysates from pLKO or Csk shRNA stable CHME3 microglial cell sub-clones (n = 3–5 cultures). Under some conditions, cells were co-transfected with YFP-FKBP and Lyn$_{11}$-FRB (CT-CID) or with YFP-FKBP-Rhoa (CA) and Lyn$_{11}$-FRB (Rhoa-CID). All groups were treated with 500 nM rapamycin for 24 h. Src was the loading control.

(K) Confocal imaging of p65-GFP-transfected (green) pLKO, Csk KD, or Src^{Y527F} stable N9 microglial cell sub-clones (n = 29–30 cells from 3 cultures). Nuclei were stained with DAPI (blue). Scale bar: 10 μm.

(L) TNF amounts (ELISA) were in the culture supernatant of pLKO (CT), Csk KD or Src^{Y527F} stable N9 microglial cell sub-clones (n = 6 cultures).

Data are represented as mean with 95% CI. *p < 0.05 (Mann-Whitney test in A, B, C, F, G, and H; two-way ANOVA in E and I; one-way ANOVA in K and L). See also Figure S4.

A

TAM TAM AZD - DMSO AZD - DMSO AZD - DMSO AZD - DMSO Analysis

P26 P28 P35 P42 P49 P56 P63-65

B DMSO AZD

Src pTyr^{416} (60 kDa)

Src (60 kDa)

Rhoa$^{fl/fl}$:Cx3cr1^{CreER+}

pSrc/Src

C # Microglia

D Iba1$^+$ cells/mm^2

E TNF mRNA expression

- Rhoa$^{fl/fl}$- DMSO
- Rhoa$^{fl/fl}$:Cx3cr1^{CreER+} - DMSO
- Rhoa$^{fl/fl}$:Cx3cr1^{CreER+} - AZD

F TNF (pg/ml)

CT, RhoA KD, RhoA KD + Src^{Y416F}, Csk KD, Csk KD + SKI-1

G Glu release

WT - CT, WT - Rhoa KD, Tnf KO - Rhoa KD

H Glu release

- CHME3 (EC$_{50}$: 53.5 pg/ml)
- N9 (EC$_{50}$: 19.4 pg/ml)
- Primary (EC$_{50}$: 177 pg/ml)

log[Tnf], pg/ml

I Glu release

Rhoa^{WT}, Rhoa^{T19N}, Rhoa^{T19N} + anti-Tnf

J Glu release

CT, Rhoa KD, Rhoa KD + SKI-1, Rhoa KD + SKI-1 + Tnf, Rhoa KD + POM, Rhoa KD + POM + Tnf, Rhoa KD + gap junction blocker, Csk KD, Src^{Y527F}

K Glu release

CT, RhoA^{Q63L}, Src CID, RhoA^{Q63L} + Src CID

L Extracellular glu (fau)

CT, RhoA KD, RhoA KD + SKI-1, Csk KD, Src^{Y527F}

M Beaded neurite/Toatal

WT - CT (MCM), WT - Rhoa KD (MCM), Tnf KO - Rhoa KD (MCM)

N Beaded neurite/Total

CT (MCM), Rhoa KD (MCM), Rhoa KD + SKI-1 (MCM), Rhoa KD + Src^{Y416F} (MCM), Rhoa KD + POM (MCM), Rhoa KD + POM +Tnf (MCM), CT + Tnf (MCM)

O RhoA^{WT} (MCM) Rhoa^{T19N} (MCM) Rhoa^{T19N} + Src^{Y416F} (MCM) Rhoa^{T19N} + anti-Tnf (ACM)

vGlut-1

PSD-95

Merge

vGlut-1$^+$/PSD-95$^+$ puncta

- RhoA^{WT} (MCM)
- Rhoa^{T19N} (MCM)
- Rhoa^{T19N} + Src^{Y416F} (MCM)
- Rhoa^{T19N} + anti-Tnf (MCM)

P Rhoa$^{fl/fl}$ DMSO Rhoa$^{fl/fl}$:Cx3cr1^{CreER+} DMSO Rhoa$^{fl/fl}$:Cx3cr1^{CreER+} AZD

vGlut-1
PSD-95

vGlut-1$^+$/PSD-95$^+$ puncta

Q Novel object exploration [Novel - Familiar (s)]

- Rhoa$^{fl/fl}$- DMSO
- Rhoa$^{fl/fl}$:Cx3cr1^{CreER+} - DMSO
- Rhoa$^{fl/fl}$:Cx3cr1^{CreER+} - AZD

(legend on next page)

Modulating Rhoa/Src Pathway in Microglia Prevents Neurodegeneration

Next, we investigated whether blocking Src would rescue, to some extent, synaptotoxicity and the associated memory deficits in Rhoa$^{fl/fl}$:Cx3cr1^{CreER+} mice. Therefore, following TAM administration, we injected Rhoa$^{fl/fl}$:Cx3cr1^{CreER+} mice weekly with the potent Src blocker AZD 0530 (Figure 4A) and 1 month later confirmed that this regimen of AZD 0530 was effective in decreasing Src activation in their brain (Figure 4B). A single intraperitoneal (i.p.) injection of AZD 0530 was sufficient to reduce Src activation in the brains of naive wild-type (WT) mice (Figure S5A) with an apparent IC$_{50}$ of approximately 0.024 mg/kg (Figure S5B), indicating that the amounts of AZD 0530 present in the brain after 1 week are sufficient to sustain Src inhibition. Src inhibition by AZD 0530 prevented the decrease of microglial numbers in Rhoa$^{fl/fl}$:Cx3cr1^{CreER+} mice (Figures 4C and 4D; Figures S5C and S5D) and the increase of mRNA transcript, of TNF in Rhoa$^{fl/fl}$:Cx3cr1^{CreER+} brains (Figure 4E).

Expressing the dominant-negative Src mutant Src^{Y416F} in Rhoa KD microglia prevented TNF release compared with Rhoa KD microglia (Figure 4F). Src^{Y416F} expression also caused a reduced activation of NF-κB in Rhoa KD microglia (Figure S5E). Pharmacological inhibition of Src, using the Src blocker SKI-1, in

Csk KD microglia also prevented TNF release (Figure 4F) and NF-κB nuclear translocation (Figure S5E).

Because blocking Src activity in microglia lacking Rhoa abrogated TNF production, we postulated that it would also inhibit glutamate release, thereby preventing microglia from becoming neurotoxic. Ablating microglial TNF (using TNF knockout [KO]) abrogated the release of glutamate triggered by depleting Rhoa (Figure 4G), and TNF dose-dependently increased the release of glutamate from CHME3 microglia, N9 microglia, and primary microglia (Figure 4H). We further confirmed that TNF released from microglia was inducing the release of glutamate by using adalimumab (a monoclonal anti-TNF blocking antibody), which blocked the release of glutamate triggered by overexpressing Rhoa^{T19N} in microglia (Figure 4I). The Src inhibitor SKI-1 attenuated the release of glutamate in Rhoa KD microglia (Figure 4J), whereas exogenous application of TNF rescued the release of glutamate after inhibiting Src in Rhoa KD microglia (Figure 4J). Preventing TNF production in Rhoa KD microglia, using the antineoplastic TNF inhibitor pomalidomide (POM), also inhibited the increase of glutamate release (Figure 4J), which could again be rescued by exogenous application of TNF (Figure 4J).

One main route for glutamate release from active microglia is its extrusion through gap junction hemichannels (Maezawa and Jin,

Figure 4. Src Inhibition Compensates Rhoa Deficiency in Microglia, Preventing Synapse Loss and Memory Deficits

(A) Regimen of 10 mg/kg AZD 0530 or DMSO injections to Rhoa$^{fl/fl}$:Cx3cr1^{CreER+} mice after TAM administration.

(B) Western blot for Src pTyr^{416} on lysates from the brains of Rhoa$^{fl/fl}$:Cx3cr1^{CreER+} mice injected with 10 mg/kg AZD 0530 or DMSO (n = 6 mice). Src was used as the loading control.

(C) Fluorescence-activated cell sorting (FACS) analysis of microglia in Rhoa$^{fl/fl}$ and Rhoa$^{fl/fl}$:Cx3cr1^{CreER+} mice injected with 10 mg/kg AZD 0530 or DMSO (n = 5-7 mice).

(D) Iba1 immunolabeling on tissue sections from the hippocampal dentate gyrus of Rhoa$^{fl/fl}$ and Rhoa$^{fl/fl}$:Cx3cr1^{CreER+} mice injected with 10 mg/kg AZD 0530 or DMSO (n = 6–7 mice).

(E) qRT-PCR from the neocortex of Rhoa$^{fl/fl}$ and Rhoa$^{fl/fl}$:Cx3cr1^{CreER+} mice injected with 10 mg/kg AZD 0530 or DMSO (n = 6–9 mice).

(F) TNF amounts (ELISA) in the culture supernatant of pLKO (CT), Rhoa KD or Rhoa KD:Src^{Y416F}, Csk KD, or Csk KD treated with SKI-1 (500 nM; 24 h) stable N9 microglial cell sub-clones (n = 3–10 cultures).

(G) Primary microglia from WT or TNF KO mice were infected with pLKO (CT) and Rhoa KD lentiviruses and then transfected with the glutamate release FRET biosensor FLIPE (n = 11–32 cells from 3 cultures).

(H) CHME3 microglia (n = 6 cells from 2 independent cultures), N9 microglia (n = 6 cells from 2 cultures), or primary microglia (n = 4 cells from 2 cultures) expressing the glutamate release FRET biosensor FLIPE were treated with different concentrations of recombinant TNF. Traced lines represent baseline glutamate release.

(I) CHME3 microglial cells were co-transfected with the Rhoa^{WT} or Rhoa^{T19N} and the glutamate release FRET biosensor FLIPE (n = 15-20 cells from 2 cultures). Cultures were then incubated with an FcR blocking solution for 10 min, and under some conditions, Rhoa^{T19N} cells were treated with adalimumab (anti-TNF; 5 μg/ml; 48 h).

(J) pLKO (CT), Rhoa KD, Csk KD, or Src^{Y527F} CHME3 microglial cell sub-clones were transfected with the glutamate release FRET biosensor FLIPE (n = 7–23 cells from 3 cultures). Under some conditions, Rhoa KD cells were treated with the Src inhibitor SKI-1 (500 nM; 24 h), the inhibitor of TNF production pomalidomide (POM; 500 nM; 24 h), recombinant TNF (30 pg/ml; 24 h), or the gap junction blocker 18-alpha- glycyrrhetinic acid (10 μM; 24 h).

(K) CHME3 microglial cells expressing the glutamate release FRET biosensor FLIPE were co-transfected with pLKO (CT) or Rhoa^{Q63L} together with RapR-Src and FRB-mCherry (n = 8–10 cells from 3 cultures) and treated with 500 nM rapamycin for 90 min.

(L) Glutamate amounts in the culture media from pLKO (CT), Rhoa KD, Csk KD, or Src^{Y527F} N9 microglial cell sub-clones (n = 4–7 cultures). Under some conditions, Rhoa KD cells were treated with the Src inhibitor SKI-1 (500 nM; 24 h).

(M) Primary hippocampal neuronal cultures expressing mVenus were incubated for 24 h with MCM obtained from primary microglia cultures from WT mice (infected with CT or Rhoa KD lentiviruses) or TNF KO mice (infected with Rhoa KD lentiviruses) (n = 3 cultures).

(N) Primary hippocampal neuronal cultures expressing mVenus were incubated for 24 h with MCM obtained from pLKO (CT), Rhoa KD, and RhoA KD + Src^{Y416F} N9 microglial cell sub-clones (n = 3–7 cultures). Under some conditions, Rhoa KD microglia were treated with SKI-1 (500 nM; 24 h) or POM (500 nM; 24 h). Recombinant TNF (30 pg/ml; 24 h) was used in CT microglial clones.

(O) vGlut-1 (green) and PSD-95 (red) immunolabelling in primary hippocampal neurons incubated for 24 h with conditioned media from CHME3 microglial cultures (MCM) overexpressing Rhoa^{WT}, Rhoa^{T19N}, or Src^{Y416F} (n = 20 neurites from 2 cultures). Microglial cultures were pre-incubated with an FcR receptor blocking solution for 20 min and in some treated with adalimumab (anti-TNF; 5 μg/ml; 48 h). Scale bar: 5 μm.

(P) vGlut-1 (green) and PSD-95 (red) immunolabeling on tissue sections from the hippocampal CA1 region of Rhoa$^{fl/fl}$ and Rhoa$^{fl/fl}$:Cx3cr1^{CreER+} mice injected with 10 mg/kg AZD 0530 or DMSO (n = 6-7 mice). Scale bar: 5 μm. Asterisks denote synaptic puncta (yellow).

(Q) DMSO- and AZD 0530-injected Rhoa$^{fl/fl}$ or Rhoa$^{fl/fl}$:Cx3cr1^{CreER+} mice were evaluated in the NOR test (n = 10-11 mice).

Data are represented as mean with 95% CI. *p < 0.05 (Mann-Whitney test in B; Kruskal-Wallis test in C–E and P; one-way ANOVA in F, G, I–O, and Q). See also Figure S5.

2010; Socodato et al., 2018). Blocking gap junctions using 18-alpha-glycyrrhetinic acid in Rhoa KD microglia prevented glutamate release (Figure 4J). In addition, hyperactivating Src (by Csk KD or by expressing Src^{Y527F}) recapitulated the effect of Rhoa KD in microglia and increased glutamate release (Figure 4J).

Increasing basal Rhoa activation in microglia by expressing Rhoa^{Q63L} was sufficient to decrease glutamate release (Figure 4K). Therefore, we hypothesized that if Src acted downstream of Rhoa to promote glutamate release, then forcing Src activation, which increases TNF production, in Rhoa^{Q63L}-expressing microglia should result in glutamate release. To test this hypothesis, we used a Src-CID strategy to exert precise temporal control over Src activation (Karginov et al., 2010). Exposing microglial cultures co-expressing RapR-Src and FRB-mCherry (Src-CID) to rapamycin led to a significant increase in glutamate release (Figure 4K) and resulted in the release of glutamate in cells expressing Rhoa^{Q63L} (Figure 4K). Rhoa KD or direct Src hyperactivation led to an accumulation of glutamate in the extracellular medium (Figure 4L). Inhibiting Src with SKI-1 in Rhoa KD microglia also abrogated the extracellular accumulation of glutamate (Figure 4L).

We assessed whether inhibiting Src or TNF after depleting Rhoa would attenuate neurite damage in hippocampal neurons. CM from TNF-deficient microglia prevented neurite beading caused by Rhoa KD (Figures 4M and S5F). Inhibiting Src in microglia (using SKI-1 or the dominant-negative Src mutant Src^{Y416F}) prevented neurite beading in cultured hippocampal neurons caused by the CM of Rhoa KD microglia (Figures 4N and S5G). CM from Rhoa KD microglia, in which TNF was inhibited with POM, also prevented neurite beading, and adding recombinant TNF to Rhoa KD microglia in the presence of POM induced neurite beading (Figures 4N and S5G). The CM of control microglia treated with TNF also led to extensive neurite beading (Figures 4N and S5G). Paralleling the effect in neurite damage, the CM from microglia overexpressing Rhoa^{T19N} produced a significant loss of synaptic puncta in primary hippocampal neurons (Figure 4O), and decreasing microglial Src activity or blocking microglial TNF significantly attenuated this effect (Figure 4O). Accordingly, Rhoa$^{fl/fl}$:Cx3cr1^{CreER+} mice injected with AZD 0530 not only contained more hippocampal excitatory synapses (Figure 4P) but also had increased amounts of the structural synaptic markers synapsin-1, synaptophysin, and PSD-95 compared with Rhoa$^{fl/fl}$:Cx3cr1^{CreER+} mice injected with vehicle (Figure S5H).

Next, we evaluated, using the NOR test, whether AZD 0530 would also attenuate memory deficits after Rhoa ablation in microglia. Rhoa$^{fl/fl}$:Cx3cr1^{CreER+} mice injected with AZD 0530 spent more time exploring the novel object (Figure 4Q) and discriminated the novel object better than Rhoa$^{fl/fl}$:Cx3cr1^{CreER+} mice injected with vehicle (Figure S5I). We observed no differences in total object exploration time between Rhoa$^{fl/fl}$:Cx3cr1^{CreER+} mice injected with AZD 0530 and controls (Figure S5J).

We did not find significant differences between DMSO-injected Cx3cr1^{CreER+}, AZD-injected Cx3cr1^{CreER+}, or Rhoa$^{fl/fl}$ mice in microglial numbers (Figure S5K), excitatory synapse number (Figure S5L), recognition memory (Figures S5M and S5N), anxiety-related behavior (Figures S5O–S5S), and locomotor activity (Figure S5T), suggesting that AZD administration did not affect these features at the steady state.

We also injected Rhoa$^{fl/fl}$:Cx3cr1^{CreER+} and control Cx3cr1^{CreER+} mice with POM (50 mg/kg i.p. 3 times per week over 4 weeks) and found that this dosage of POM decreased the expression of TNF in the brains of Cx3cr1^{CreER+} and Rhoa$^{fl/fl}$:Cx3cr1^{CreER+} mice (Figure S5U). Besides decreasing brain TNF expression, POM administration also significantly prevented the decrease of vGlut-1$^+$/PSD95$^+$ synapses in Rhoa$^{fl/fl}$:Cx3cr1^{CreER+} mice (Figure S5V), suggesting that the increased TNF expression was, at least in part, involved in the synapse loss elicited by the ablation of Rhoa in microglia.

Rhoa Ablation in Microglia Produces an Amyloid-like Pathology

Together with synapse loss, LTP impairment, and memory deficits (Figure 2), deposition of amyloid beta (Aβ) underlies multiple CNS neurodegenerative states, including AD. Ablation of Rhoa in microglia resulted in increased amounts of Aβ (Figure 5A) and its amyloidogenic precursor β-CTF (a carboxyl-terminal fragment generated by the cleavage of APP (amyloid precursor protein) by β-secretases; Figure 5B) in Rhoa$^{fl/fl}$:Cx3cr1^{CreER+} brains. Total APP levels were comparable between genotypes (Figure 5B). Corroborating the increased amyloidogenic processing of APP, we detected increased amounts of Aβ$_{1-40}$ peptide and of Aβ$_{1-42}$ peptide in Rhoa$^{fl/fl}$:Cx3cr1^{CreER+} brains (Figure 5C). We also found that the excess of Aβ formed fibrillar plaque-like structures (labeled by methoxy-X04) in the neocortex of Rhoa$^{fl/fl}$:Cx3cr1^{CreER+} mice but not in Rhoa$^{fl/fl}$ neocortices (Figure 5D).

Production of Aβ by neurons is in large part activity dependent (Cirrito et al., 2005) and induced by the activation of glutamate receptors (Lesné et al., 2005). As decreasing Rhoa activity in microglia enhanced glutamate secretion, we investigated whether this increase modulated the production of Aβ by neurons. The CM from microglia overexpressing the dominant-negative Rhoa mutant Rhoa^{T19N} induced a significant increase of Aβ42 in primary hippocampal neurons (Figure 5E). This effect was abrogated by decreasing microglial Src activity or by neutralizing microglial TNF (Figure 5E).

Aβ Oligomers Induce Microglia Neurotoxic Polarization by Decreasing Rhoa Activity

Our results in Rhoa$^{fl/fl}$:Cx3cr1^{CreER+} mice suggest that microglia dysregulation drives amyloidogenic processing of APP, leading to an increased production of Aβ by neurons, but could Aβ signal back to microglia and alter Rhoa activity? Using APP/PS1 mice (Borchelt et al., 1997), in which Aβ is abundantly produced and secreted by neurons, we found a significant decrease of Rhoa activation (GTP-Rhoa) and of Csk expression and an increase of Src activation in APP/PS1 microglia (Figure 5F). No significant differences were found in the numbers of microglia, brain macrophages, and blood monocytes (Figures S6A and S6B) or in the percentages of brain macrophages and blood monocytes expressing GTP-Rhoa, Csk, or Src Tyr^{416} phosphorylation (Figures S6C and S6D) between 4-month-old APP/PS1 and WT littermates.

Next, we investigated whether application of little amounts (200 nM) of Aβ$_{1-42}$ oligomers could indeed modulate Rhoa signaling in microglia. We found by FRET, using the Raichu-Rhoa biosensor (Yoshizaki et al., 2003), that Rhoa activity in
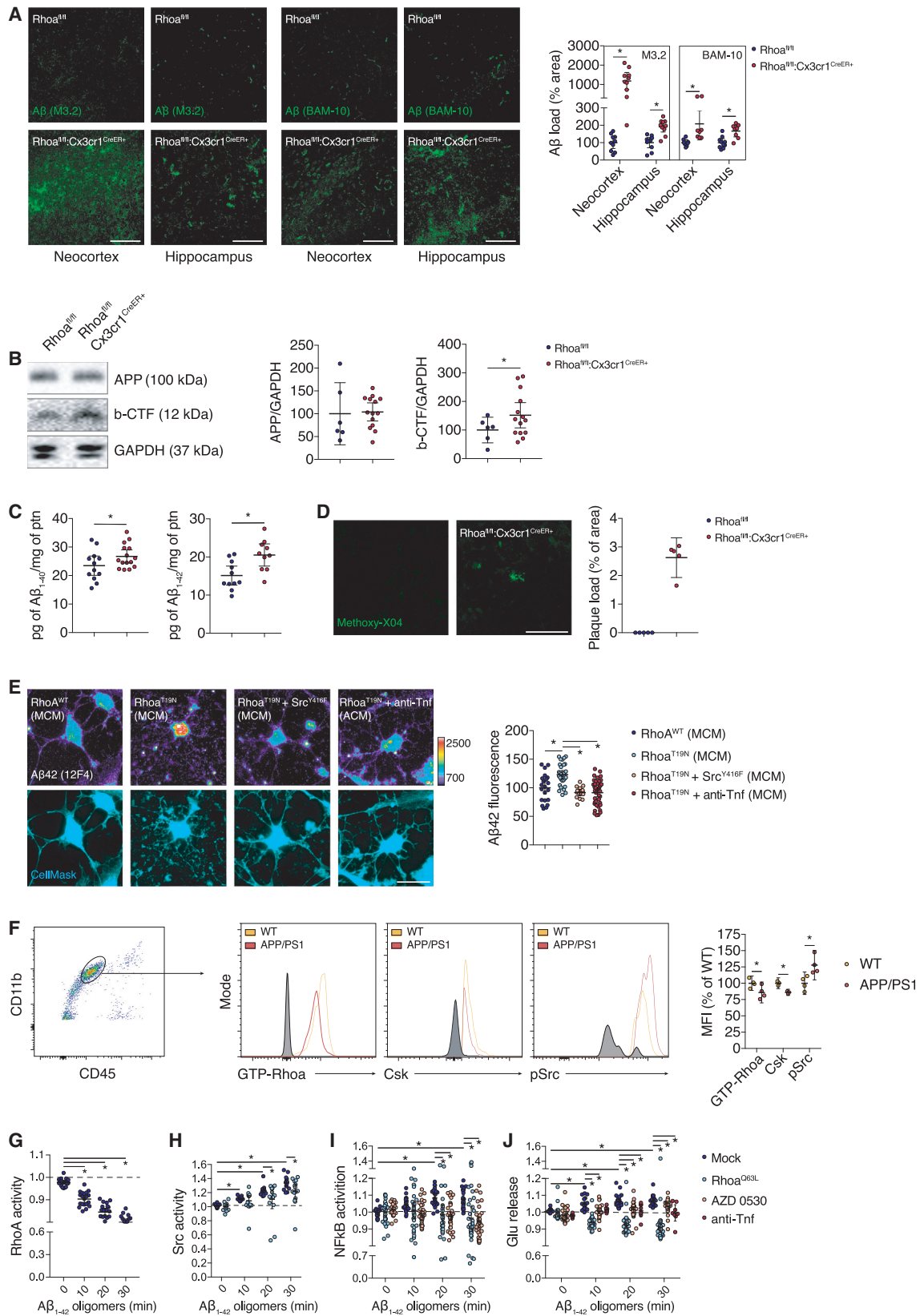
living microglia decreased following exposure to Aβ$_{1-42}$ oligomers (Figure 5G). Conversely, Src activity at the plasma membrane (visualized by FRET with the KRas Src YPet biosensor) increased (Figure 5H), and expression of the constitutively active Rhoa mutant Rhoa^{Q63L} significantly attenuated this effect (Figure 5H).

Using the pIκBα-miRFP703 biosensor to detect the activation of canonical NF-κB pathway (Shcherbakova et al., 2016), we also observed that exposure to Aβ$_{1-42}$ oligomers induced time-dependent activation of the NF-κB pathway in living microglia (Figure 5I) and overexpressing Rhoa^{Q63L} or blocking Src with AZD 0530 abrogated this effect (Figure 5I). Finally, using the FLIPE biosensor, we observed by FRET that exposure to Aβ$_{1-42}$ oligomers increased glutamate release from living microglia in a time-dependent manner (Figure 5J), an effect inhibited by Rhoa^{Q63L}, by AZD 0530, and by neutralizing TNF with adalimumab (Figure 5J). These data suggest that Aβ oligomers can signal back to microglia and decrease Rhoa activation, providing a positive feedback loop for Src hyperactivation and TNF-dependent glutamate release.

Blocking Src Decreases Amyloid-like Pathology in Microglia Rhoa-Deficient Mice

Next, we investigated if inhibiting Src would modulate the reactivity of microglia in early-depositing APP/PS1 mice. Of note, a single i.p. injection of AZD 0530 in APP/PS1 mice was sufficient to decrease Src activity in their brains (Figure S6E). Therefore, and as we did for Rhoa$^{fl/fl}$:Cx3cr1^{CreER+} mice, we blocked Src activity by giving AZD 0530 weekly to 3-month-old APP/PS1 mice for 1 month (Figure S6F) and investigated whether Src inhibition would preserve hippocampal synapses. Injecting AZD 0530 in APP/PS1 mice substantially inhibited the decrease of vGlut-1$^+$/PSD-95$^+$ synapses (Figure S6G). Concurrent with the idea that Src inhibition decreases microglia activation, we found increased microglial ramification in the neocortex of APP/PS1 mice injected with AZD 0530 (Figure S6H). Paralleling this increased microglial ramification in APP/PS1 mice treated with

AZD 0530, we also observed an increase in the ramification of microglia following Src inhibition with AZD 0530 in Rhoa$^{fl/fl}$:Cx3cr1^{CreER+} mice (Figure S6I).

Plaque-associated microglia restrict amyloid plaque formation, limiting pathology in AD mouse models by phagocytosis of amyloid deposits (Wang et al., 2015). We thus investigated whether Rhoa activation and consequent blockade of Src would improve microglial engulfment of Aβ. Chemogenetic activation of Rhoa using the Rhoa-CID strategy significantly increased the uptake of Aβ$_{1-42}$ by microglia (Figure 6A). Activation of Rhoa led to Src inhibition, and accordingly, blockade of Src with AZD 0530 also increased Aβ$_{1-42}$ uptake by microglia (Figure 6B). Blocking Src with AZD 0530 significantly increased microglia engulfment of Aβ deposits in brains of both APP/PS1 (Figure S6J) and Rhoa$^{fl/fl}$:Cx3cr1^{CreER+} mice (Figures 6C and S6K). AZD 0530 treatment caused no significant alterations in the amounts of APP either in APP/PS1 or in Rhoa$^{fl/fl}$:Cx3cr1^{CreER+} mice (Figures S6L and S6M), indicating that AZD 0530 does not impact APP production.

Paralleling the increased Aβ clearance by microglia, we observed a significant decrease of amyloid burden (Aβ amounts detected using BAM-10 and E610 antibodies) in the brain of APP/PS1 mice injected with AZD 0530 (Figures S6N and S6O). AZD 0530 also decreased Aβ deposition (Figures 6D and S6P), the production of both Aβ$_{1-40}$ and Aβ$_{1-42}$ peptides (Figure 6E), and the formation of fibrillar plaque-like structures labeled by methoxy-X04 (Figure 6F) in the neocortex of Rhoa$^{fl/fl}$:Cx3cr1^{CreER+} mice, indicating that blockade of Src downstream of Rhoa mitigates amyloid burden.

DISCUSSION

Crossing Cx3cr1$^{CreER-EYFP}$ mice (Parkhurst et al., 2013) with Rhoa floxed mice (Herzog et al., 2011; Jackson et al., 2011) allowed us to study the role of Rhoa in adult brain microglia and circumvented some limitations of previous studies that used overexpression of Rhoa dominant mutants (Bianchi et al., 2011; Ohsawa et al.,

---

Figure 5. Loss of Rhoa in Adult Microglia Produces an Amyloid-like Pathology

(A) Confocal images of Aβ deposits in Rhoa$^{fl/fl}$ and Rhoa$^{fl/fl}$:Cx3cr1^{CreER+} mice 50 days post-TAM (n = 7 mice for BAM-10 and 10 mice for M3.2). Scale bars: 100 μm.

(B) Western blot using M3.2 antibody (detecting APP and β-CTF) on lysates from the brains of Rhoa$^{fl/fl}$ and Rhoa$^{fl/fl}$:Cx3cr1^{CreER+} 50 days post-TAM (n = 6–14 mice). GAPDH was the loading control.

(C) ELISA for Aβ$_{1-40}$ and Aβ$_{1-42}$ on neocortical extracts of RhoA$^{fl/fl}$ and RhoA$^{fl/fl}$:Cx3cr1^{CreER+} 50 days post-TAM (n = 12–15 mice for Aβ$_{1-40}$ and n = 10–11 mice for Aβ$_{1-42}$).

(D) Confocal images of methoxy-X04$^+$ plaque-like deposits on RhoA$^{fl/fl}$ and RhoA$^{fl/fl}$:Cx3cr1^{CreER+} neocortices 50 days post-TAM (n = 5 mice).

(E) Intracellular endogenous Aβ42 (immunolabeled with anti-Aβ42 clone 12F4) and CellMask dye (cyan) in primary hippocampal neurons incubated for 24 h with MCM overexpressing Rhoa^{WT}, Rhoa^{T19N}, or Src^{Y416F} (n = 15–40 cells from 2 cultures). Microglial cultures were pre-incubated with an FcR receptor blocking solution for 20 min and in some conditions also treated with adalimumab (anti-TNF; 5 μg/ml; 48 h). Scale bar: 20 μm.

(F) Flow cytometry showing expression of GTP-Rhoa, Csk, or Src pTyr^{416} in microglia (gated using CD45^{mid}CD11b$^+$) from 4-month-old WT and APP/PS1 mice (n = 3–4 mice).

(G) CHME3 microglia expressing a RhoA FRET activity biosensor were recorded in saline before (t = 0 min) and after treatment with 200 nM Aβ$_{1-42}$ oligomers (n = 20 cells from 3 cultures).

(H) CHME3 microglia expressing a Src FRET activity biosensor were mock transfected or transfected with RhoA^{Q63L} and then recorded in saline before (t = 0 min) and after treatment with 200 nM Aβ$_{1-42}$ oligomers (n = 15–16 cells from 3 cultures).

(I and J) CHME3 microglia expressing a biosensor to measure NF-κB pathway activation (I) or a glutamate release FRET biosensor (J) were mock transfected (n = 23–25 from 3 cultures) or transfected with RhoA^{Q63L} (n = 39 cells from 3 cultures) or incubated with AZD 0530 (200 nM; 1 h; n = 31–34 cells from 3 cultures) or pre-incubated with FcR blocker (20 min), followed by treatment with adalimumab (anti-TNF; 5 μg/ml; 48 h; n = 8 cells from 2 cultures), and then recorded in saline before (t = 0 min) and after treatment with 200 nM Aβ$_{1-42}$ oligomers.

Data are represented as mean with 95% CI. *p < 0.05 (unpaired t test in A–C and F; one-way ANOVA in E; two-way ANOVA in G–J). See also Figure S6.
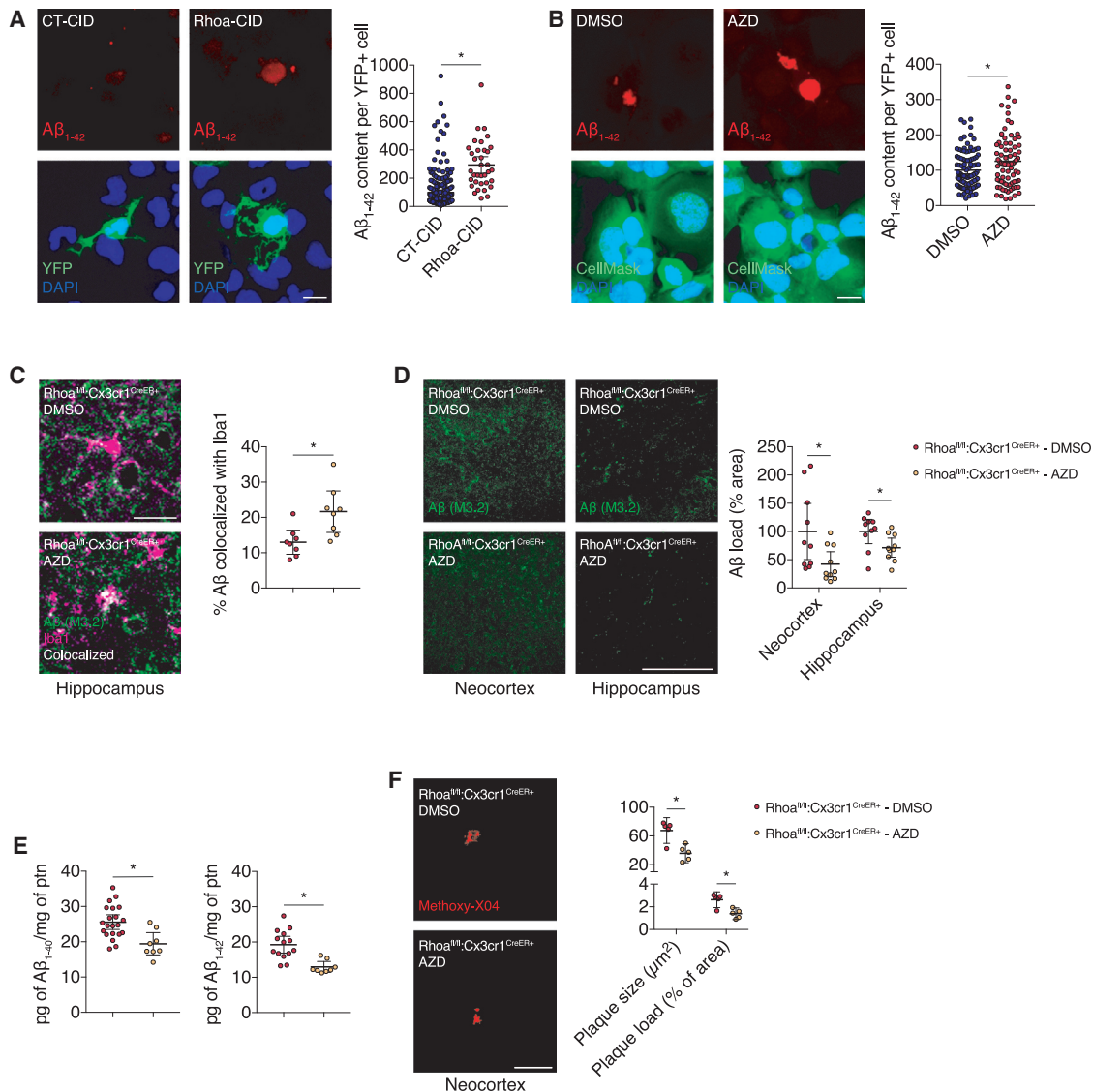
Figure 6. Src Inhibition Mitigates the Amyloid-like Pathology Elicited by the Loss of Rhoa in Adult Microglia

(A) CHME3 microglia were co-transfected with YFP-FKBP and Lyn$_{11}$-FRB or with YFP-FKBP-Rhoa (CA) and Lyn$_{11}$-FRB (n = 211–395 cells from 3 cultures). All cells were treated with Aβ$_{1-42}$ fluorescent particles (10 μg/ml) and rapamycin (500 nM) for 90 min.

(B) CHME3 microglia (stained with CellMask dye; green) were treated with or AZD 0530 (n = 89–113 cells from 3 cultures) and incubated with Aβ$_{1-42}$ fluorescent particles (10 μg/ml) for 90 min.

(C) Confocal images showing colocalization (white) of Iba1$^+$ microglia with M3.2 immunoreactive amyloid deposits on tissue sections from Rhoa$^{fl/fl}$:Cx3cr1^{CreER+} mice (hippocampus) injected with 10 mg/kg AZD 0530 or DMSO (n = 8 mice). Scale bars: 10 μm.

(D) Confocal images showing M3.2$^+$ amyloid deposits on tissue sections from Rhoa$^{fl/fl}$:Cx3cr1^{CreER+} mice injected with 10 mg/kg AZD 0530 or DMSO (n = 10 animals mice). Scale bars: 200 μm.

(E) ELISA for Aβ$_{1-40}$ and Aβ$_{1-42}$ on neocortical extracts of RhoA$^{fl/fl}$:Cx3cr1^{CreER+} mice injected with 10 mg/kg AZD 0530 or DMSO (n = 8–21 animals for Aβ$_{1-40}$ and n = 8–14 animals for Aβ$_{1-42}$).

(F) Confocal images of methoxy-X04$^+$ plaque-like deposits on neocortices RhoA$^{fl/fl}$:Cx3cr1^{CreER+} mice injected with 10 mg/kg AZD 0530 or DMSO (n = 5 mice). Scale bar: 50 μm.

Data are represented as mean with 95% CI. *p < 0.05 (Mann-Whitney test in A–D and F; unpaired t test in E). See also Figure S6.

2000; Moon et al., 2013), which may trigger off-target and trans-dominant effects (Zhou and Zheng, 2013; Wang and Zheng, 2007), as well as the use of C3 exoenzyme toxin (Rattan et al., 2003; Hoffmann et al., 2008), which inhibits not only Rhoa but also Rhob and Rhoc (Mohr et al., 1992; Chardin et al., 1989).

Rhoa works through multiple downstream pathways and effectors, and it is to be expected that the loss of Rhoa might disturb the functions and/or interactions of more than one of its effectors. For example, knocking out Rhoa in the mouse spinal cord neuroepithelium does not cause cytokinesis defects

(Herzog et al., 2011), whereas knocking out the Rhoa effector citron-kinase impairs cytokinesis (Di Cunto et al., 2000). This could also explain why Rhoa deficiency activates microglia, whereas the pharmacological inhibition of the Rhoa effector Rho-kinase (ROCK) does not (Mueller et al., 2005; Chen et al., 2013). Another factor potentially contributing to the disparity of these 2 phenotypes is that, in addition of being activated by Rhoa, ROCK can also be regulated by Rhoe/Rnd3 (Riento et al., 2003) or by Rhoc (Riento and Ridley, 2003). Our data, however, suggested that Rhoc did not play a significant role in microglia proinflammatory activation and microglia-induced neurotoxicity.

ROCK inhibition by Y27632 or fasudil attenuates microglia activation, promoting some functional recovery in animal models for different neurological conditions (Mueller et al., 2005; Chen et al., 2013; Chong et al., 2017, Sellers et al., 2018). Because Rhoa is likely to exert its control over microglia immune activity through several other downstream effectors besides ROCK, for which activation can also be regulated independently of Rhoa (Julian and Olson, 2014), these studies are not very informative concerning Rhoa regulation of microglial function. In addition, Y27632 and fasudil are not cell specific and have substantial off-target effects (Vigil and Der, 2013), making it difficult to attribute any phenotype solely to the inhibition of ROCK downstream of Rhoa.

Excessive secretion of glutamate by microglia can induce excitotoxic neuronal damage (Maezawa and Jin, 2010; Takeuchi et al., 2006) and, by exacerbating neuronal activity, can also increase the production of Aβ species by neurons (Lesné et al., 2005). Blocking TNF, and the consequent release of glutamate, from microglia lacking Rhoa prevented neurite damage and also the increase of Aβ42 in primary hippocampal neurons. Injecting POM (a brain penetrant immunomodulatory agent that also inhibits TNF expression) in Rhoa mutant mice decreased brain TNF expression and attenuated synapse loss. Although POM might have inhibited other pathways in addition to TNF, our *in vitro* data demonstrated that TNF signaling was required for neurite beading and synapse loss, suggesting that TNF contributed to the synapse loss following Rhoa ablation in microglia.

AZD 0530 inhibits SFK phosphorylation, including Fyn, Src, Lyn, and other family members. Although AZD 0530 inhibits Src more potently than other SFK (for example the reported IC$_{50}$ for Src is 2.7 nM, whereas that for Fyn is around 10 nM; Green et al., 2009), and despite of our compelling *in vitro* results pointing out a key and rather specific role of Src in driving the phenotype produced by depleting Rhoa in microglia, we cannot claim that, *in vivo*, the only kinase inhibited was Src. This is also applicable to the work of Kaufman et al. (2015), who report that the effect of AZD 0530 in diminishing some aspects of AD-like pathology in APP/PS1 mice is due to decreased Fyn activation in neurons. It is likely that besides inhibiting Fyn in neurons, AZD 0530 might also inhibit other SFKs in neurons and in other brain cell types, including Src in microglia. Accordingly, and in the context of our work, we cannot therefore exclude that the effect of AZD 0530 in preventing synapse loss and decreasing the amyloid burden in Rhoa mutants and in APP/PS1 mice was contributed, at least in part, by SFK inhibition in both glia and neurons.

The dose-response curve of AZD 0530 revealed an apparent IC$_{50}$ of 0.024 mg/kg for Src inhibition in the brain. AZD 0530 has a half-life of 16 h in the brain (Kaufman et al., 2015); therefore, around 0.0146 mg/kg (10.5 half-lives) of AZD 0530 will remain in the brain following our administration protocol. Because the lowest dose of AZD 0530 (0.002 mg/kg) we tested produced around 30% of Src inhibition, these data show that the dosage of AZD 0530 we used effectively sustained Src inhibition in the brain, which is in accordance with a persistent effect of AZD 0530 reported for APP/PS1 mice after drug washout (Smith et al., 2018).

We observed decreased Rhoa activity in microglia obtained from early-depositing APP/PS1 mice, a stage in which synapse loss was already present without robust amyloid pathology, suggesting that such a decrease in Rhoa activation might have contributed to the synapse loss in early-depositing APP/PS1 mice. Indeed, blocking Src, downstream of Rhoa, prevented synapse loss, increased microglial engulfment of Aβ, and decreased Aβ burden. However, substantial glial activation driven by overexpressing proinflammatory cytokines can also decrease amyloid burden in AD mice (Chakrabarty et al., 2010, 2011), casting doubts whether attenuating microglial activation per se would be sufficient to preserve synapses as amyloid pathology builds up during the course of AD.

Loss of synapses, LTP impairment, recognition memory deficits, and deposition of Aβ are consistent hallmarks found in human AD patients and in animal models of AD. Similarly, Rhoa ablation in adult microglia reproduced some of these hallmarks, further supporting the hypothesis that disrupting Rhoa signaling produces spontaneous microglia activation, leading to neurodegeneration. In this regard, our data provide additional validation to the notion of "microgliopathy" (Prinz and Priller, 2014), in which microglia dysfunction, by itself, could initiate or be a major cause of neurological disease.

STAR★METHODS

Detailed methods are provided in the online version of this paper and include the following:

- KEY RESOURCES TABLE
- RESOURCE AVAILABILITY
  - Lead Contact
  - Materials Availability
  - Data and Code Availability
- EXPERIMENTAL MODEL AND SUBJECT DETAILS
  - Animals
  - Conditional Rhoa-deficient mice
  - Tnf deficient mice
  - AD mice
  - Primary cultures of hippocampal neurons
  - Primary cultures of cortical microglia
  - Microglial cell lines
- METHOD DETAILS
  - Flow cytometry and cell sorting
  - MACS isolation of adult microglia
  - Brain tissue preparation and immunofluorescence
  - Image reconstruction and morphometric analysis

- ○ NeuN quantification
- ○ Quantification of amyloid deposits
- ○ APP quantification
- ○ Methoxy-X04 quantification
- ○ Quantification of synapses
- ○ TUNEL assay
- ○ Quantification of Iba1 colocalization with amyloid deposits
- ○ Immunofluorescence on cultured microglia
- ○ Time-lapse video microscopy and FRET assays
- ○ Preparation of lysates (tissue and cell cultures)
- ○ Enzyme-linked immunosorbent assay (ELISA)
- ○ Glutamate determination by fluorimetry
- ○ Nuclear and cytosolic fractionation
- ○ Western blotting
- ○ Electrophysiology
- ○ Behavioral tests
- ○ Elevated plus-maze (EPM)
- ○ Open field (OF)
- ○ Novel object recognition (NOR)
- ○ Cloning of shRNAs into pSicoR-GFP vector
- ○ Lentiviruses/Retroviruses production
- ○ Total RNA extraction, cDNA synthesis and qRT-PCR
- ○ Preparation of Aβ oligomers
- ○ $A\beta_{1-42}$ uptake assay
- ● QUANTIFICATION AND STATISTICAL ANALYSIS

SUPPLEMENTAL INFORMATION

Supplemental Information can be found online at https://doi.org/10.1016/j.celrep.2020.107796.

AUTHOR CONTRIBUTIONS

Conceptualization, R.S., C.C.P., and J.B.R.; Methodology, R.S. and C.C.P.; Investigation, R.S., C.C.P., T.C., A.R., T.O.A., J.F.H., S.H.V., J.M., C.M.S., F.I.B., R.L.A., V.C.-S., A.P.S., and A.M.; Writing – Original Draft, R.S., C.C.P., A.P.S., R.P.-d.-C., C.B., A.M.S., T.S., A.F.A., and J.B.R.; Writing – Review & Editing, R.S., C.C.P., and J.B.R.; Funding Acquisition, A.F.A. and J.B.R.; Supervision, J.B.R.

DECLARATION OF INTERESTS

The authors declare no competing interests.

REFERENCES

abd-el-Basset, E., and Fedoroff, S. (1995). Effect of bacterial wall lipopolysaccharide (LPS) on morphology, motility, and cytoskeletal organization of microglia in cultures. J. Neurosci. Res. *41*, 222–237.

Albensi, B.C., Oliver, D.R., Toupin, J., and Odero, G. (2007). Electrical stimulation protocols for hippocampal synaptic plasticity and neuronal hyper-excitability: are they effective or relevant? Exp. Neurol. *204*, 1–13.

Anderson, W.W., and Collingridge, G.L. (2001). The LTP Program: a data acquisition program for on-line analysis of long-term potentiation and other synaptic events. J. Neurosci. Methods *108*, 71–83.

Bianchi, R., Kastrisianaki, E., Giambanco, I., and Donato, R. (2011). S100B protein stimulates microglia migration via RAGE-dependent up-regulation of chemokine expression and release. J. Biol. Chem. *286*, 7214–7226.

Block, M.L., Zecca, L., and Hong, J.S. (2007). Microglia-mediated neurotoxicity: uncovering the molecular mechanisms. Nat. Rev. Neurosci. *8*, 57–69.

Borchelt, D.R., Ratovitski, T., van Lare, J., Lee, M.K., Gonzales, V., Jenkins, N.A., Copeland, N.G., Price, D.L., and Sisodia, S.S. (1997). Accelerated amyloid deposition in the brains of transgenic mice coexpressing mutant presenilin 1 and amyloid precursor proteins. Neuron *19*, 939–945.

Bustelo, X.R., Sauzeau, V., and Berenjeno, I.M. (2007). GTP-binding proteins of the Rho/Rac family: regulation, effectors and functions in vivo. BioEssays *29*, 356–370.

Chakrabarty, P., Jansen-West, K., Beccard, A., Ceballos-Diaz, C., Levites, Y., Verbeeck, C., Zubair, A.C., Dickson, D., Golde, T.E., and Das, P. (2010). Massive gliosis induced by interleukin-6 suppresses Abeta deposition in vivo: evidence against inflammation as a driving force for amyloid deposition. FASEB J. *24*, 548–559.

Chakrabarty, P., Herring, A., Ceballos-Diaz, C., Das, P., and Golde, T.E. (2011). Hippocampal expression of murine TNFα results in attenuation of amyloid deposition in vivo. Mol. Neurodegener. *6*, 16.

Chardin, P., Boquet, P., Madaule, P., Popoff, M.R., Rubin, E.J., and Gill, D.M. (1989). The mammalian G protein rhoC is ADP-ribosylated by Clostridium botulinum exoenzyme C3 and affects actin microfilaments in Vero cells. EMBO J. *8*, 1087–1092.

Chen, M., Liu, A., Ouyang, Y., Huang, Y., Chao, X., and Pi, R. (2013). Fasudil and its analogs: a new powerful weapon in the long war against central nervous system disorders? Expert Opin. Investig. Drugs *22*, 537–550.

Chong, C.M., Ai, N., and Lee, S.M. (2017). ROCK in CNS: Different Roles of Isoforms and Therapeutic Target for Neurodegenerative Disorders. Curr. Drug Targets *18*, 455–462.

Cirrito, J.R., Yamada, K.A., Finn, M.B., Sloviter, R.S., Bales, K.R., May, P.C., Schoepp, D.D., Paul, S.M., Mennerick, S., and Holtzman, D.M. (2005). Synaptic activity regulates interstitial fluid amyloid-beta levels in vivo. Neuron *48*, 913–922.

Crotti, A., and Ransohoff, R.M. (2016). Microglial Physiology and Pathophysiology: Insights from Genome-wide Transcriptional Profiling. Immunity *44*, 505–515.

Deczkowska, A., Amit, I., and Schwartz, M. (2018). Microglial immune checkpoint mechanisms. Nat. Neurosci. *21*, 779–786.

DeGeer, J., and Lamarche-Vane, N. (2013). Rho GTPases in neurodegeneration diseases. Exp. Cell Res. *319*, 2384–2394.

Di Cunto, F., Imarisio, S., Hirsch, E., Broccoli, V., Bulfone, A., Migheli, A., Atzori, C., Turco, E., Triolo, R., Dotto, G.P., et al. (2000). Defective neurogenesis in citron kinase knockout mice by altered cytokinesis and massive apoptosis. Neuron *28*, 115–127.

Droppelmann, C.A., Campos-Melo, D., Volkening, K., and Strong, M.J. (2014). The emerging role of guanine nucleotide exchange factors in ALS and other neurodegenerative diseases. Front. Cell. Neurosci. *8*, 282.

Ennaceur, A., Michalikova, S., Bradford, A., and Ahmed, S. (2005). Detailed analysis of the behavior of Lister and Wistar rats in anxiety, object recognition and object location tasks. Behav. Brain Res. *159*, 247–266.

Ferreira, T.A., Blackman, A.V., Oyrer, J., Jayabal, S., Chung, A.J., Watt, A.J., Sjöström, P.J., and van Meyel, D.J. (2014). Neuronal morphometry directly from bitmap images. Nat. Methods *11*, 982–984.

Ginhoux, F., Greter, M., Leboeuf, M., Nandi, S., See, P., Gokhan, S., Mehler, M.F., Conway, S.J., Ng, L.G., Stanley, E.R., et al. (2010). Fate mapping analysis reveals that adult microglia derive from primitive macrophages. Science *330*, 841–845.

Goldmann, T., Wieghofer, P., Müller, P.F., Wolf, Y., Varol, D., Yona, S., Brendecke, S.M., Kierdorf, K., Staszewski, O., Datta, M., et al. (2013). A new type of microglia gene targeting shows TAK1 to be pivotal in CNS autoimmune inflammation. Nat. Neurosci. *16*, 1618–1626.

Goldmann, T., Wieghofer, P., Jordão, M.J., Prutek, F., Hagemeyer, N., Frenzel, K., Amann, L., Staszewski, O., Kierdorf, K., Krueger, M., et al. (2016). Origin, fate and dynamics of macrophages at central nervous system interfaces. Nat. Immunol. *17*, 797–805.

Gómez-Nicola, D., Fransen, N.L., Suzzi, S., and Perry, V.H. (2013). Regulation of microglial proliferation during chronic neurodegeneration. J. Neurosci. *33*, 2481–2493.

Green, T.P., Fennell, M., Whittaker, R., Curwen, J., Jacobs, V., Allen, J., Logie, A., Hargreaves, J., Hickinson, D.M., Wilkinson, R.W., et al. (2009). Preclinical anticancer activity of the potent, oral Src inhibitor AZD0530. Mol. Oncol. *3*, 248–261.

Herzog, D., Loetscher, P., van Hengel, J., Knüsel, S., Brakebusch, C., Taylor, V., Suter, U., and Relvas, J.B. (2011). The small GTPase RhoA is required to maintain spinal cord neuroepithelium organization and the neural stem cell pool. J. Neurosci. *31*, 5120–5130.

Hodge, R.G., and Ridley, A.J. (2016). Regulating Rho GTPases and their regulators. Nat. Rev. Mol. Cell Biol. *17*, 496–510.

Hoffmann, A., Hofmann, F., Just, I., Lehnardt, S., Hanisch, U.K., Brück, W., Kettenmann, H., Ahnert-Hilger, G., and Höltje, M. (2008). Inhibition of Rho-dependent pathways by Clostridium botulinum C3 protein induces a proinflammatory profile in microglia. Glia *56*, 1162–1175.

Inoue, T., Heo, W.D., Grimley, J.S., Wandless, T.J., and Meyer, T. (2005). An inducible translocation strategy to rapidly activate and inhibit small GTPase signaling pathways. Nat. Methods *2*, 415–418.

Jackson, B., Peyrollier, K., Pedersen, E., Basse, A., Karlsson, R., Wang, Z., Lefever, T., Ochsenbein, A.M., Schmidt, G., Aktories, K., et al. (2011). RhoA is dispensable for skin development, but crucial for contraction and directed migration of keratinocytes. Mol. Biol. Cell *22*, 593–605.

Janabi, N., Peudenier, S., Héron, B., Ng, K.H., and Tardieu, M. (1995). Establishment of human microglial cell lines after transfection of primary cultures of embryonic microglial cells with the SV40 large T antigen. Neurosci. Lett. *195*, 105–108.

Julian, L., and Olson, M.F. (2014). Rho-associated coiled-coil containing kinases (ROCK): structure, regulation, and functions. Small GTPases *5*, e29846.

Jung, S., Aliberti, J., Graemmel, P., Sunshine, M.J., Kreutzberg, G.W., Sher, A., and Littman, D.R. (2000). Analysis of fractalkine receptor CX(3)CR1 function by targeted deletion and green fluorescent protein reporter gene insertion. Mol. Cell. Biol. *20*, 4106–4114.

Karginov, A.V., Ding, F., Kota, P., Dokholyan, N.V., and Hahn, K.M. (2010). Engineered allosteric activation of kinases in living cells. Nat. Biotechnol. *28*, 743–747.

Kaufman, A.C., Salazar, S.V., Haas, L.T., Yang, J., Kostylev, M.A., Jeng, A.T., Robinson, S.A., Gunther, E.C., van Dyck, C.H., Nygaard, H.B., and Strittmatter, S.M. (2015). Fyn inhibition rescues established memory and synapse loss in Alzheimer mice. Ann. Neurol. *77*, 953–971.

Kaur, C. (1997). Effects of colchicine on amoeboid microglial cells in the postnatal rat brain. Arch. Histol. Cytol. *60*, 453–462.

Kierdorf, K., Erny, D., Goldmann, T., Sander, V., Schulz, C., Perdiguero, E.G., Wieghofer, P., Heinrich, A., Riemke, P., Hölscher, C., et al. (2013). Microglia emerge from erythromyeloid precursors via Pu.1- and Irf8-dependent pathways. Nat. Neurosci. *16*, 273–280.

Leger, M., Quiedeville, A., Bouet, V., Haelewyn, B., Boulouard, M., Schumann-Bard, P., and Freret, T. (2013). Object recognition test in mice. Nat. Protoc. *8*, 2531–2537.

Lesné, S., Ali, C., Gabriel, C., Croci, N., MacKenzie, E.T., Glabe, C.G., Plotkine, M., Marchand-Verrecchia, C., Vivien, D., and Buisson, A. (2005). NMDA receptor activation inhibits alpha-secretase and promotes neuronal amyloid-beta production. J. Neurosci. *25*, 9367–9377.

Maezawa, I., and Jin, L.W. (2010). Rett syndrome microglia damage dendrites and synapses by the elevated release of glutamate. J. Neurosci. *30*, 5346–5356.

Mejía-García, T.A., Portugal, C.C., Encarnação, T.G., Prado, M.A., and Paes-de-Carvalho, R. (2013). Nitric oxide regulates AKT phosphorylation and nuclear translocation in cultured retinal cells. Cell. Signal. *25*, 2424–2439.

Mohr, C., Koch, G., Just, I., and Aktories, K. (1992). ADP-ribosylation by Clostridium botulinum C3 exoenzyme increases steady-state GTPase activities of recombinant rhoA and rhoB proteins. FEBS Lett. *297*, 95–99.

Moon, M.Y., Kim, H.J., Li, Y., Kim, J.G., Jeon, Y.J., Won, H.Y., Kim, J.S., Kwon, H.Y., Choi, I.G., Ro, E., et al. (2013). Involvement of small GTPase RhoA in the regulation of superoxide production in BV2 cells in response to fibrillar Aβ peptides. Cell. Signal. *25*, 1861–1869.

Mueller, B.K., Mack, H., and Teusch, N. (2005). Rho kinase, a promising drug target for neurological disorders. Nat. Rev. Drug Discov. *4*, 387–398.

Nada, S., Okada, M., MacAuley, A., Cooper, J.A., and Nakagawa, H. (1991). Cloning of a complementary DNA for a protein-tyrosine kinase that specifically phosphorylates a negative regulatory site of p60c-src. Nature *351*, 69–72.

Ohsawa, K., Imai, Y., Kanazawa, H., Sasaki, Y., and Kohsaka, S. (2000). Involvement of Iba1 in membrane ruffling and phagocytosis of macrophages/microglia. J. Cell Sci. *113*, 3073–3084.

Okumoto, S., Looger, L.L., Micheva, K.D., Reimer, R.J., Smith, S.J., and Frommer, W.B. (2005). Detection of glutamate release from neurons by genetically encoded surface-displayed FRET nanosensors. Proc. Natl. Acad. Sci. USA *102*, 8740–8745.

Palop, J.J., Chin, J., and Mucke, L. (2006). A network dysfunction perspective on neurodegenerative diseases. Nature *443*, 768–773.

Parkhurst, C.N., Yang, G., Ninan, I., Savas, J.N., Yates, J.R., 3rd, Lafaille, J.J., Hempstead, B.L., Littman, D.R., and Gan, W.-B. (2013). Microglia promote learning-dependent synapse formation through brain-derived neurotrophic factor. Cell *155*, 1596–1609.

Portugal, C.C., Socodato, R., Canedo, T., Silva, C.M., Martins, T., Coreixas, V.S., Loiola, E.C., Gess, B., Röhr, D., Santiago, A.R., et al. (2017). Caveolin-1-mediated internalization of the vitamin C transporter SVCT2 in microglia triggers an inflammatory phenotype. Sci. Signal. *10*, eaal2005.

Prinz, M., and Priller, J. (2014). Microglia and brain macrophages in the molecular age: from origin to neuropsychiatric disease. Nat. Rev. Neurosci. *15*, 300–312.

Rattan, R., Giri, S., Singh, A.K., and Singh, I. (2003). Rho A negatively regulates cytokine-mediated inducible nitric oxide synthase expression in brain-derived transformed cell lines: negative regulation of IKKalpha. Free Radic. Biol. Med. *35*, 1037–1050.

Rice, R.A., Spangenberg, E.E., Yamate-Morgan, H., Lee, R.J., Arora, R.P., Hernandez, M.X., Tenner, A.J., West, B.L., and Green, K.N. (2015). Elimination of Microglia Improves Functional Outcomes Following Extensive Neuronal Loss in the Hippocampus. J. Neurosci. *35*, 9977–9989.

Riento, K., and Ridley, A.J. (2003). Rocks: multifunctional kinases in cell behaviour. Nat. Rev. Mol. Cell Biol. *4*, 446–456.

Riento, K., Guasch, R.M., Garg, R., Jin, B., and Ridley, A.J. (2003). RhoE binds to ROCK I and inhibits downstream signaling. Mol. Cell. Biol. *23*, 4219–4229.

Righi, M., Mori, L., De Libero, G., Sironi, M., Biondi, A., Mantovani, A., Donini, S.D., and Ricciardi-Castagnoli, P. (1989). Monokine production by microglial cell clones. Eur. J. Immunol. *19*, 1443–1448.

Schulz, C., Gomez Perdiguero, E., Chorro, L., Szabo-Rogers, H., Cagnard, N., Kierdorf, K., Prinz, M., Wu, B., Jacobsen, S.E., Pollard, J.W., et al. (2012). A lineage of myeloid cells independent of Myb and hematopoietic stem cells. Science *336*, 86–90.

Sellers, K.J., Elliott, C., Jackson, J., Ghosh, A., Ribe, E., Rojo, A.I., Jarosz-Griffiths, H.H., Watson, I.A., Xia, W., Semenov, M., et al. (2018). Amyloid β synaptotoxicity is Wnt-PCP dependent and blocked by fasudil. Alzheimers Dement. *14*, 306–317.

Shcherbakova, D.M., Baloban, M., Emelyanov, A.V., Brenowitz, M., Guo, P., and Verkhusha, V.V. (2016). Bright monomeric near-infrared fluorescent proteins as tags and biosensors for multiscale imaging. Nat. Commun. *7*, 12405.

Silva, C.S., Eira, J., Ribeiro, C.A., Oliveira, Â., Sousa, M.M., Cardoso, I., and Liz, M.A. (2017). Transthyretin neuroprotection in Alzheimer's disease is dependent on proteolysis. Neurobiol. Aging *59*, 10–14.

Smith, L.M., Zhu, R., and Strittmatter, S.M. (2018). Disease-modifying benefit of Fyn blockade persists after washout in mouse Alzheimer's model. Neuropharmacology *130*, 54–61.

Socodato, R., Santiago, F.N., Portugal, C.C., Domingues, A.F., Santiago, A.R., Relvas, J.B., Ambrósio, A.F., and Paes-De-Carvalho, R. (2012). Calcium-permeable AMPA Receptors trigger neuronal NOS activation to promote nerve cell death in an Src kinase-dependent fashion. J. Biol. Chem. *287*, 38680–38694.

Socodato, R., Portugal, C.C., Canedo, T., Domith, I., Oliveira, N.A., Paes-de-Carvalho, R., Relvas, J.B., and Cossenza, M. (2015a). c-Src deactivation by the polyphenol 3-O-caffeoylquinic acid abrogates reactive oxygen species-mediated glutamate release from microglia and neuronal excitotoxicity. Free Radic. Biol. Med. *79*, 45–55.

Socodato, R., Portugal, C.C., Domith, I., Oliveira, N.A., Coreixas, V.S., Loiola, E.C., Martins, T., Santiago, A.R., Paes-De-Carvalho, R., Ambrosio, A.F., and Relvas, J.B. (2015b). c-Src function is necessary and sufficient for triggering microglial cell activation. Glia *63*, 497–511.

Socodato, R., Portugal, C.C., Rodrigues, A., Henriques, J., Rodrigues, C., Figueira, C., and Relvas, J.B. (2018). Redox tuning of Ca²⁺ signaling in microglia drives glutamate release during hypoxia. Free Radic. Biol. Med. *118*, 137–149.

Spangenberg, E.E., Lee, R.J., Najafi, A.R., Rice, R.A., Elmore, M.R., Blurton-Jones, M., West, B.L., and Green, K.N. (2016). Eliminating microglia in Alzheimer's mice prevents neuronal loss without modulating amyloid-β pathology. Brain *139*, 1265–1281.

Stankiewicz, T.R., and Linseman, D.A. (2014). Rho family GTPases: key players in neuronal development, neuronal survival, and neurodegeneration. Front. Cell. Neurosci. *8*, 314.

Takeuchi, H., Jin, S., Wang, J., Zhang, G., Kawanokuchi, J., Kuno, R., Sonobe, Y., Mizuno, T., and Suzumura, A. (2006). Tumor necrosis factor-alpha induces neurotoxicity via glutamate release from hemichannels of activated microglia in an autocrine manner. J. Biol. Chem. *281*, 21362–21368.

Thomas, R.M., Schmedt, C., Novelli, M., Choi, B.K., Skok, J., Tarakhovsky, A., and Roes, J. (2004). C-terminal SRC kinase controls acute inflammation and granulocyte adhesion. Immunity *20*, 181–191.

Ventura, A., Meissner, A., Dillon, C.P., McManus, M., Sharp, P.A., Van Parijs, L., Jaenisch, R., and Jacks, T. (2004). Cre-lox-regulated conditional RNA interference from transgenes. Proc. Natl. Acad. Sci. USA *101*, 10380–10385.

Vigil, D., and Der, C.J. (2013). Inhibitors of the ROCK serine/threonine kinases: key effectors of the RhoA small GTPase. Enzymes *33 Pt A*, 193–212.

Wang, L., and Zheng, Y. (2007). Cell type-specific functions of Rho GTPases revealed by gene targeting in mice. Trends Cell Biol. *17*, 58–64.

Wang, Y., Cella, M., Mallinson, K., Ulrich, J.D., Young, K.L., Robinette, M.L., Gilfillan, S., Krishnan, G.M., Sudhakar, S., Zinselmeyer, B.H., et al. (2015). TREM2 lipid sensing sustains the microglial response in an Alzheimer's disease model. Cell *160*, 1061–1071.

Wheeler, A.P., and Ridley, A.J. (2004). Why three Rho proteins? RhoA, RhoB, RhoC, and cell motility. Exp. Cell Res. *301*, 43–49.

Yona, S., Kim, K.W., Wolf, Y., Mildner, A., Varol, D., Breker, M., Strauss-Ayali, D., Viukov, S., Guilliams, M., Misharin, A., et al. (2013). Fate mapping reveals origins and dynamics of monocytes and tissue macrophages under homeostasis. Immunity *38*, 79–91.

Yoshizaki, H., Ohba, Y., Kurokawa, K., Itoh, R.E., Nakamura, T., Mochizuki, N., Nagashima, K., and Matsuda, M. (2003). Activity of Rho-family GTPases during cell division as visualized with FRET-based probes. J. Cell Biol. *162*, 223–232.

Yu, Z., Cheng, G., Wen, X., Wu, G.D., Lee, W.T., and Pleasure, D. (2002). Tumor necrosis factor alpha increases neuronal vulnerability to excitotoxic necrosis by inducing expression of the AMPA-glutamate receptor subunit GluR1 via an acid sphingomyelinase- and NF-kappaB-dependent mechanism. Neurobiol. Dis. *11*, 199–213.

Zhou, X., and Zheng, Y. (2013). Cell type-specific signaling function of RhoA GTPase: lessons from mouse gene targeting. J. Biol. Chem. *288*, 36179–36188.

STAR★METHODS

KEY RESOURCES TABLE

REAGENT or RESOURCE	SOURCE	IDENTIFIER
Antibodies		
Rhoa antibody	Abcam	Cat#ab86297; RID:AB_10675086
RhoA (67B9) antibody	Cell Signaling Technology	Cat#2117; RRID:AB_10693922
Active RhoA-GTP antibody	NewEast Biosciences	Cat#26904; RRID:AB_1961799
Src antibody [EPR5496]	Abcam	Cat#ab109381; RRID:AB_10865528
Amyloid beta precursor protein antibody [Y188]	Abcam	Cat#ab32136; RRID:AB_2289606
GFP antibody	Abcam	Cat#ab6673; RRID:AB_305643
Anti-NeuN antibody	Millipore	Cat#MAB377; RRID:AB_2298772
Phospho-Src Family (Tyr416) (D49G4) Rabbit mAb antibody	Cell Signaling Technology	Cat#6943; RRID:AB_10013641
Phospho-Src Family (Tyr416) Antibody	Cell Signaling Technology	Cat#2101; RRID:AB_331697
NF- κB p65 (L8F6) Mouse mAb antibody	Cell Signaling Technology	Cat#6956; RRID:AB_10828935
Csk (C74C1) Rabbit mAb antibody	Cell Signaling Technology	Cat#498; RRID:AB_2276592
Rabbit Anti-PSD95 Monoclonal Antibody, Unconjugated, Clone D74D3	Cell Signaling Technology	Cat#3409; RRID:AB_1264242
PSD95 Monoclonal Antibody (6G6-1C9)	Thermo Fisher Scientific	Cat#MA1-045; RRID:AB_325399
Anti Iba1, Rabbit antibody	Wako	Cat#019-19741; RRID:AB_839504
Mouse Anti-Glyceraldehyde-3-Phosphate Dehydrogenase (GAPDH) Antibody, Unconjugated	Hytest	Cat#5G4-9B3; RRID:AB_1616725
Mouse Anti-beta-Actin Monoclonal Antibody, Unconjugated, Clone AC-74	Sigma-Aldrich	Cat#A2228; RRID:AB_476697
Monoclonal Anti-Synaptophysin antibody produced in mouse	Sigma-Aldrich	Cat#S5768; RRID:AB_477523
Mouse Anti-beta-Amyloid Protein Monoclonal Antibody, Unconjugated, Clone BAM-10	Sigma-Aldrich	Cat#A5213; RRID:AB_476742
VGLUT 1 (vesicular glutamate transporter 1, BNPI, SLC17A7) antibody	Synaptic Systems	Cat#135 303; RRID:AB_887875
Anti-Synapsin 1 antibody	Synaptic Systems	Cat#106 011C5; RRID:AB_993033
Purified anti-mouse/rat β-Amyloid, 1-16 antibody	BioLegend	Cat#805707; RRID:AB_2734556
Purified anti-β-Amyloid, 1-16 antibody	BioLegend	Cat#803004; RRID:AB_2715854
Purified anti-β-Amyloid, 1-42 antibody	BioLegend	Cat#805509; RRID:AB_2783381
LAMP1, mAb (Ly1C6) antibody	Enzo Life Sciences	Cat#ADI-VAM-EN001; RRID:AB_10630197
Anti-Histone H3, CT, pan antibody	Millipore	Cat#07-690; RRID:AB_417398
PE anti-mouse CD45 antibody	BioLegend	Cat#103106; RRID:AB_312971
APC anti-mouse/human CD11b antibody	BioLegend	Cat#101212; RRID:AB_312795
Alexa Fluor® 647 anti-mouse/human CD11b antibody	BioLegend	Cat#101218; RRID:AB_389327
PerCP/Cyanine5.5 anti-mouse Ly-6C antibody	BioLegend	Cat#128012;RRID:AB_1659241
Goat Anti-Mouse IgG (H+L) Antibody, Alexa Fluor 568 Conjugated	Molecular Probes	Cat#A-11004; RRID:AB_2534072

(*Continued on next page*)

Continued

REAGENT or RESOURCE	SOURCE	IDENTIFIER
Goat Anti-Rabbit IgG (H+L) Antibody, Alexa Fluor 568 Conjugated	Molecular Probes	Cat#A-11011; RRID:AB_143157
Goat anti-Mouse IgG (H+L) Secondary Antibody, Alexa Fluor® 594 conjugate	Thermo Fisher Scientific	Cat#A-11005; RRID:AB_2534073
Goat anti-Rabbit IgG (H+L) Secondary Antibody, Alexa Fluor® 594 conjugate	Thermo Fisher Scientific	Cat#A-11012; RRID:AB_2534079
Goat anti-Mouse IgG (H+L) Highly Cross-Adsorbed Secondary Antibody, Alexa Fluor Plus 647	Thermo Fisher Scientific	Cat#A32728; RRID:AB_2633277
Goat anti-Rabbit IgG (H+L) Cross-Adsorbed Secondary Antibody, Alexa Fluor 647	Thermo Fisher Scientific	Cat#A-21244; RRID:AB_2535812
Peroxidase-AffiniPure Donkey Anti-Rabbit IgG (H+L) (min X Bov,Ck,Gt,GP,Sy Hms,Hrs,Hu,Ms,Rat,Shp Sr Prot) antibody	Jackson ImmunoResearch Labs	Cat#711-035-152; RRID:AB_10015282
Peroxidase-AffiniPure Donkey Anti-Mouse IgG (H+L) (min X Bov,Ck,Gt,GP,Sy Hms,Hrs,Hu,Rb,Rat,Shp Sr Prot) antibody	Jackson ImmunoResearch Labs	Cat#715-035-151; RRID:AB_2340771
Adalimumab	Selleckchem	Cat#A2010
CD11b MicroBeads, human and mouse	Miltenyi Biotech	Cat#130-049-601
PE/Cy7 Annexin V	BioLegend	Cat#640950
Ki-67 antibody	Abcam	Cat#ab15580; RRID:AB_443209
Monoclonal Anti-beta-Amyloid antibody produced in mouse	Sigma-Aldrich	Cat#A5213; RRID:AB_476742
PE/Cy7 anti-mouse/human CD11b antibody	BioLegend	Cat#101215; RRID:AB_312798
PE/Cy7 anti-mouse CD192 (CCR2) Antibody	BioLegend	Cat#150611; RRID:AB_2616983
Fc Receptor Blocking Solution	BioLegend	Cat#422302; RRID:AB_2818986
Bacterial and Virus Strains		
Subcloning Efficiency DH5α Competent Cells	Thermo Fisher Scientific	Cat#18265017
Chemicals, Peptides, and Recombinant Proteins		
Recombinant Murine GM-CSF	Peprotech	Cat#315-03
Recombinant Human TNF-α	Peprotech	Cat#300-01A
Recombinant Murine TNF-α	Peprotech	Cat#315-01A
Amyloid β Protein Fragment 1-42	Sigma-Aldrich	Cat#A9810; CAS Number 107761-42-2
Beta - Amyloid (1 - 42), HiLyte™ Fluor 555 - labeled, Human	AnaSpec, Inc	Cat#AS-60480-01
Lipopolysaccharide (LPS) from *Escherichia coli* 0111:B4	Sigma-Aldrich	Cat#L2630; MDL number MFCD00164401
Src Inhibitor-1	Sigma-Aldrich	Cat#S2075; CAS Number: 179248-59-0
Rapamycin	Sigma-Aldrich	Cat#R8781
18α-Glycyrrhetinic acid	Sigma-Aldrich	Cat#G8503; CAS Number 1449-05-4
Tamoxifen	Sigma-Aldrich	Cat#T5648; CAS Number 10540-29-1
Pomalidomide	Selleckchem	Cat#S1567; CAS Number 19171-19-8
Saracatinib (AZD0530)	Selleckchem	Cat#S1006; CAS Number 379231-04-6
Recombinant Murine M-CSF	Peprotech	Cat#315-02
Zombie Violet Fixable Viability Kit	BioLegend	Cat#423114
Methoxy-X04	Tocris	Cat#4920; CAS Number 863918-78-9

Continued

REAGENT or RESOURCE	SOURCE	IDENTIFIER
Critical Commercial Assays		
Amyloid beta 40 Mouse ELISA Kit	Thermo Fisher Scientific	Cat#KMB3481
Murine TNF-α Standard ABTS ELISA Development Kit	Peprotech	Cat#900-K54
Amyloid beta 42 Mouse ELISA Kit	Thermo Fisher Scientific	Cat#KMB3441
Pierce ECL Western Blotting Substrate	Thermo Fisher Scientific	Cat#32106
Thermo Scientific SuperSignal West Pico Chemiluminescent Substrate	Thermo Fisher Scientific	Cat#10481755
ABTS ELISA Buffer Kit	Peprotech	Cat#900-K00
Experimental Models: Cell Lines		
CHME3 cell line (distributed as HMC3 cells)	ATCC	Cat#CRL-3304; RRID:CVCL_II76
N9 cell line	Prof. Claudia Verderio, CNR Institute of Neuroscience, Cellular and Molecular Pharmacology, Milan, Italy	RRID:CVCL_0452
Experimental Models: Organisms/Strains		
Mouse: Rhoa$^{fl/fl}$:Cx3cr1^{CreER+}	This work	N/A
Mouse: TNF knock out	Prof. Rui Applelberg, Universtity of Porto	N/A
Mouse: B6;C3-Tg(APP695)3Dbo Tg(PSEN1)5Dbo/Mmjax (herein APP/PS1)	The Jackson Laboratory	RRID:MMRRC_041848-JAX
Mouse: B6.129P2(Cg)-Cx3cr1$^{tm2.1(cre/ERT2)}$^{Litt}/WganJ (herein Cx3cr1$^{CreER-EYFP}$)	The Jackson Laboratory	Cat#JAX:021160; RRID:IMSR_JAX:021160
Mouse: Rhoa^{tm1Jrel} (herein Rhoa$^{fl/fl}$)	MGI	MGI:4950374
Oligonucleotides		
Primers	See Table S1	N/A
Oligos for pSicoR cloning	See Table S1	N/A
shRNA oligos	See Table S1	N/A
Recombinant DNA		
pTriEx-RhoA FLARE.sc Biosensor Q63L	PMID:16547516	RRID:Addgene_12151
pRK5-myc-RhoA-Q63L	Gary Bokoch (unpublished)	RRID:Addgene_12964
pRK5-myc-RhoA-T19N	Gary Bokoch (unpublished)	RRID:Addgene_12963
pRK5-myc-RhoA-wt	Gary Bokoch (unpublished)	RRID:Addgene_12962
pUSE-RapR-Src-myc	PMID:20581846	RRID:Addgene_25933
pDisplay FLIPE-600n	PMID:15939876	RRID:Addgene_13545
pIκBα-miRFP703	PMID:27539380	RRID:Addgene_80005
psPAX2	Didier Trono (unpublished)	RRID:Addgene_12260
pMD2.G	Didier Trono (unpublished)	RRID:Addgene_12259
pUMVC	PMID:12649500	RRID:Addgene_8449
GFP-RelA	PMID:11533489	RRID:Addgene_23255
MSCV	PMID:20008935	RRID:Addgene_24828
pSicoR	PMID:15240889	RRID:Addgene_11579
YF-RhoA(CA)	PMID:15908919	RRID:Addgene_20153
YFP-FKBP (YF)	PMID:15908919	RRID:Addgene_20175
Lyn11-targeted FRB (LDR)	PMID:15908919	RRID:Addgene_20147
pCherry-FRB	PMID:20581846	RRID:Addgene_25920
mCherry-Lifeact-7	Michael Davidson (unpublished)	RRID:Addgene_54491
RhoC FLARE.sc mCer, mVenus - wt	PMID:24224016	RRID:Addgene_65071
Kras-Src FRET biosensor	PMID:18799748	RRID:Addgene_78302
Raichu-RhoA	Michiyuki Matsuda; PMID:12860967	N/A
pLNCX chick src Y416F	Joan Brugge (unpublished)	RRID:Addgene_13662

(Continued on next page)

Continued

REAGENT or RESOURCE	SOURCE	IDENTIFIER
pLNCX chick src Y527F	Joan Brugge (unpublished)	RRID:Addgene_13660
pLNCX chick src	Joan Brugge (unpublished)	RRID:Addgene_13665
pTriEx-RhoA FLARE.sc Biosensor WT	PMID:16547516	RRID:Addgene_12150
pTriEx-RhoA FLARE.sc Biosensor T19N	PMID:16547516	RRID:Addgene_12152
pFRET-HSP33 cys	Ulrich Hammerling (unpublished)	RRID:Addgene_16076
Software and Algorithms		
Fiji	PMID:22743772	RRID:SCR_002285
GraphPad Prism	https://www.graphpad.com/	RRID:SCR_002798
Adobe Illustrator	https://www.adobe.com/products/illustrator.html	RRID:SCR_010279
Sholl analysis plugin for ImageJ	PMID:25264773 (distributed with Fiji; https://imagej.net/Downloads)	N/A
FlowJo	https://www.flowjo.com/solutions/flowjo	RRID:SCR_008520

RESOURCE AVAILABILITY

Lead Contact
Further information and requests for resources and reagents should be directed to and will be fulfilled by the Lead Contact, João Relvas (jrelvas@ibmc.up.pt).

Materials Availability
This study did not generate new unique reagents.

Data and Code Availability
This study did not generate any unique codes.

EXPERIMENTAL MODEL AND SUBJECT DETAILS

Animals
All mice experiments were reviewed by i3S animal ethical committee and were approved by Direção-Geral de Alimentação e Veterinária (DGAV). Animals were maintained in standard laboratory conditions with inverted 12h/12h light dark cycle and were allowed free access to food and water. Animals were group-housed under specific pathogen-free conditions. Experiments were carried out in adult mice (2-3 months of age) following the 3Rs ethics.

Conditional Rhoa-deficient mice
All mice experiments were approved by Direção-Geral de Alimentação e Veterinária (DGAV). Cx3cr1[CreER-EYFP] mice were purchased from Jackson Laboratories. In such mice, the *Cx3cr1* promoter drives high expression of the CreER cassette in microglia (Parkhurst et al., 2013). Mice homozygous for the *Rhoa* floxed allele (Herzog et al., 2011; Jackson et al., 2011) were backcrossed at least for 10 generations and were kept in C57BL/6 background at the I3S animal facility. All genotypes were determined by PCR on genomic DNA. Primers used for Rhoa floxed alleles were: AGC CAG CCT CTT GAC CGA TTT A (forward); TGT GGG ATA CCG TTT GAG CAT (reverse). Primers for CreER insertion were: AAG ACT CAC GTG GAC CTG CT (WT forward); AGG ATG TTG ACT TCC GAG TG (WT reverse); CGG TTA TTC AAC TTG CAC CA (mutant reverse).

Rhoa floxed mice were crossed with Cx3cr1[CreER-EYFP] mice. Progeny of interest were: Control (Rhoa^{fl/fl}) and mutants (Rhoa^{fl/fl}:Cx3cr1[CreER+]). Mice were given tamoxifen (10 mg *per* animal by oral gavage) at P26 and P28 and then analyzed at different time points (specified on the figure legends). All experiments were performed on mice kept on a C57BL/6 background. For electrophysiological recordings and in behavioral tests only male Rhoa^{fl/fl}, Cx3cr1[CreER+] and Rhoa^{fl/fl}:Cx3cr1[CreER+] littermates were used. No differences in the mRNA expression levels of Rhoa were found in FACS-sorted microglia between the brains of Rhoa^{fl/fl} - and wild-type mice after TAM administration. In addition, after TAM administration, Rhoa^{fl/fl} mice displayed no overt difference in the behavioral performance on motor, anxiety-related and memory tests when compared to wild-type mice. Administration of AZD 0530 (used at a final concentration of 10 mg/kg via IP injections; 1 IP per week lasting 4 weeks) to Rhoa^{fl/fl}:Cx3cr1[CreER+] and Rhoa^{fl/fl} mice started 1 week after the second TAM pulse. Administration of pomalidomide (used at a final concentration of 50 mg/kg via IP injections; 3 IPs per week lasting 4 weeks) to Rhoa^{fl/fl}:Cx3cr1[CreER+] and Cx3cr1[CreER+] mice started 1 week after the second TAM pulse.

Tnf deficient mice

Prof. Rui Applelberg (University of Porto) supplied C57BL/6.Tnf knockout (referred herein as Tnf KO) mice. Tnf KO mice were genotyped by PCR using ATC CGC GAC GTG GAA CTG GCA GAA (forward) and CTG CCC GGA CTC CGC AAA GTC TAA (reverse) primer pair. Tnf KO mice display a single band of 2 kb in the PCR gel. Mice were bred at i3S animal facility. Tnf KO animals were bred to maintain maximal heterozygosity.

AD mice

The AβPPswe/PS1A246E (termed APP/PS1) AD mice model co-expresses a chimeric mouse-human amyloid-β protein precursor (AβPP) bearing a human Aβ domain with mutations (K595N and M596L) linked to Swedish familial AD pedigrees and human presenilin-1 A246E mutation, with both transgenes under the control of the mouse prion protein promoter (Borchelt et al., 1997). This AD mouse model displays age-dependent and region-specific amyloidosis, gliosis and associated hippocampal-dependent memory deficits, resembling the AD pathology found in human patients (Borchelt et al., 1997). APP/PS1 mice were genotyped by PCR using PSEN primers: AAT AGA GAA CGG CAG GAG CA (forward) and GCC ATG AGG GCA CTA ATC AT (reverse); APP primers: GAC TGA CCA CTC GAC CAG GTT CTG (forward) and CTT GTA AGT TGG ATT CTC ATA TCC G (reverse); WT primers: CCT CTT TGT GAC TAT GGT GAC TGA TGT CGG (forward) and GTG GAT AAC CCC TCC CCC AGC CTA GAC C (reverse). APP/PS1 mice were maintained in SV129 background and were bred at the i3S animal facility. Administration of AZD 0530 (used at a final concentration of 20 mg/kg via IP injections; 1 IP per week lasting 4 weeks) to APP/PS1 mice started when animals completed 3 months of age.

Primary cultures of hippocampal neurons

Hippocampi were dissected from embryonic day 18 Wistar rat embryos and dissociated using trypsin (0.25%, v/v). Neurons were plated at a final density of 1×10^4 to 5×10^4 cells per dish and cultured in the presence of a glial feeder layer. Cells were cultured in Neurobasal medium supplemented with B27 supplement (1:50, v/v), 25 mM glutamate, 0.5 mM glutamine, and gentamicin (0.12 mg/ml). To prevent glial overgrowth, neuronal cultures were treated with 5 mM cytosine arabinoside after 3 days *in vitro* (DIV) and maintained in a humidified incubator with 5% CO_2/95% air at 37°C for up to 2 weeks, feeding the cells once per week by replacing one-third of the medium. To assess neurite beading, hippocampal neurons expressing mVenus were observed under a fluorescence microscope after 24 h of incubation with 50% (v/v) microglia conditioned media. Neurons were observed blindly in three independent hippocampal cultures. The ratio of bead-bearing mVenus+ neurons was calculated over the total mVenus+ neurons counted.

Primary cultures of cortical microglia

Primary cortical microglial cell cultures were performed as previously described (Socodato et al., 2015a, 2015b; Portugal et al., 2017). In brief, mice pups (2-day-old) were sacrificed, their cerebral cortices were dissected in HBSS, pH 7.2, and digested with 0.07% trypsin plus 50 μL (w/v) DNase for 15 min. Next, cells were gently dissociated using a glass pipette in DMEM F12 GlutaMAX-I supplemented with 10% FBS, 0.1% gentamicin. Cells were plated in poly-D-lysine-coated T-flasks (75 cm²) at 1.5×10^6 cells per cm². Cultures were kept at 37°C and 95% air/5% CO_2 in a humidified incubator. Culture media was changed every 3 days up to 21 days. To obtain purified microglial cell cultures, culture flasks were subjected to orbital shaking at 200 rpm for 2 h. Next, culture supernatant was collected to tubes, centrifuged at 453 g for 5 min at room temperature. The supernatant was discarded and the pellet, containing microglia, was re-suspended in culture medium, and cells were seeded in poly-D-lysine-coated 6 or 12-well culture plates at 2.5×10^5 cells/cm² with DMEM F12 GlutaMAX-I supplemented with 10% FBS, 0.1% gentamicin and 1 ng/ml M-CSF or 1 ng/ml GM-CSF. Purified microglia were cultured for 5-8 days. Immunolabeling with CD11b showed a purity of 95%–99% for these cultures.

Microglial cell lines

The microglial cell line N9 was obtained by immortalization of primary cultures from the ventral mesencephalon and cerebral cortex from ED12-13 CD1 mouse embryos with the 3RV retrovirus carrying an activated v-myc oncogene (Righi et al., 1989). Cells were cultured in RPMI 1640 supplemented with 5% FBS, 23.8mM sodium bicarbonate, 30mM D-Glucose, 100 U/mL penicillin and 100 μg/mL streptomycin, and were maintained at 37°C, 95% air and 5% CO_2 in a humidified incubator.

The microglial cell line CHME3 was obtained from primary cultures of human embryonic microglial cells by transfection with a plasmid encoding for the large T antigen of SV40 (Janabi et al., 1995). These cells were cultivated with DMEM GlutaMAX-I supplemented with 10% FBS and 100 U/mL penicillin and 100 μ/mL streptomycin, and were maintained at 37°C, 95% air and 5% CO_2 in a humidified incubator.

For generation of microglial stable cell sub-clones, N9 or CHME3 cultures were infected with viral particles and allowed to grow for additional 48h. Cultures were then selected using puromycin as before (Socodato et al., 2015b; Portugal et al., 2017). Stable cell sub-clones carrying an empty vector (pLKO) or the insert of interest were validated by western blotting or by qRT-PCR.

Primary microglial cells, N9 and CHME3 microglial cell lines were transfected using jetPRIME® (Polyplus Transfection) according to the manufacturer's protocol.

METHOD DETAILS

Flow cytometry and cell sorting

For characterization of microglia and macrophages in the samples, the following markers were used: CD45-PE, CD11b-APC, CD11b-Alexa Fluor 647, CCR2-PE/Cy7 and Ly6C-PerCP/Cy5.5. Microglial and macrophages were collected from the tissues (brain, blood and spleen) of control and mutant mice using density gradient separation. In brief, mice were anesthetized and then perfused with ice-cold PBS. For single cell suspensions, tissues were quickly dissected, placed on ice-cold RPMI and mechanically homogenized. Cell suspension was passed through a 100 μm cell strainer and centrifuged over a discontinuous 70%/30% Percoll gradient. Cells on the interface were collected, pelleted, washed extensively and then counted in a Neubauer chamber using trypan blue exclusion to estimate the number of live cells. Single cell suspensions (5×10^5 cells) were incubated with different mixes of FACS antibodies for 30 min at 4°C in the dark. Compensation settings were determined using spleen from both control and mutant. Cell suspensions were evaluated on a FACS Canto II analyzer (BD Immunocytometry Systems). For intracellular staining, cell suspensions were run over Percoll gradient, washed and counted as above. Afterward, cells were seeded in a U bottom 96-well plate and incubated with CD45-PE, CD11b-Alexa Fluor 647 or CD11b-PE/Cy7. After antibody washing, cells were fixed in 2% PFA for 30 min, washed in PBS and permeabilized with permeabilization buffer (Life Technologies 00-8333-56). Intracellular antibody staining mix was prepared in permeabilization buffer and incubated with the cells overnight at 4°C in the dark. After washing in permeabilization buffer, cells were incubated with Alexa Fluor 488 or 647 secondary antibody for 1 h at 25°C in the dark. After that, cells were washed twice in permeabilization buffer, washed twice in FACS staining buffer (2% BSA, 0.1% sodium azide in PBS) and analyzed in FACS Canto II. Fluorescence minus one controls for Rhoa, GTP-Rhoa, Csk and phospho-Src were prepared in mixes with CD45-PE and CD11b-Alexa Fluor 647 CD11b-PE/Cy7 plus secondary antibodies alone. Cell sorting was performed on a FACS ARIA cell sorter. Data were analyzed by FlowJo X10 software (TreeStar).

MACS isolation of adult microglia

Mice were sacrificed in a CO_2 chamber and the brains were removed. The right hemisphere was mechanically dissociated in ice-cold Dounce buffer (15mM HEPES; 0,5% Glucose; and DNase in PBS) by 6 strokes in a tissue potter. Then, the homogenate was passed through a 70 μm cell strainer, centrifuged and cells were counted in a TC10 Automated Cell Counter from BIO-RAD using Trypan Blue to exclude dead cells. 4×10^7 cells were pelleted by centrifugation (9300 g; 1 min; 4°C) and resuspended in 360 μL of MACS Buffer (0.5% BSA; 2 mM EDTA in PBS) followed by incubation with 40 μL CD11b Microbeads (130-093-634 Miltenyi Biotec). CD11b$^+$ fraction was selected using LS columns (130-042-401 Miltenyi Biotec) in a MACS separator (Miltenyi Biotec) according to the manufacture's instructions. Eluted CD11b enriched fraction was centrifuged (9300 g; 1 min; 4°C), the pellet was lysed in RIPA-DTT buffer and used for protein isolation.

Brain tissue preparation and immunofluorescence

After animal perfusion with ice-cold PBS (15 ml) and fixation by perfusion with 4% PFA, brains were post-fixed by immersion in 4% PFA in PBS, pH 7.4 overnight. After that, brains were washed with PBS and then cryoprotected using sucrose gradient in a row (15 and 30%). After 24 h, brains were mounted in OCT embedding medium, frozen and cryosectioned in the CM3050S Cryostat (Leica Biosystems). Coronal sections from brains (30 μm thickness between bregma positions 1.0 mm and −2.0 mm) were collected non-sequentially on Superfrost ultra plus slides. Brain sections from control and from mutant mice encompassing identical stereological regions were collected on the same glass slide. Slides were stored at −20°C until processed for immunohistochemistry.

Frozen sections were defrosted by at least 1 h and hydrated with PBS for 15 min. Sections were permeabilized with 0.25% Triton X-100 for 15 min, washed with PBS for 10 min and blocked (5% BSA, 5% FBS, 0.1% Triton X-100) for 1 h. Primary antibodies were incubated in blocking solution in a humidified chamber overnight at 4°C. Secondary antibodies were incubated for 2 h in blocking solution. After the secondary antibody, sections were washed three times for 10 min with PBS and incubated for 10 min with DAPI and rinsed twice in PBS. Slides were coverslipped using glycergel or Immumount and visualized under a Leica TCS SP5 II confocal microscope.

Image reconstruction and morphometric analysis

Images from tissue sections were acquired using a Leica HC PL APO Lbl. Blue 20x /0.70 IMM/CORR or a Leica HC PL APO CS 40x /1.10 CORR water objective in 8-bit sequential mode using standard TCS mode at 400 Hz and the pinhole was kept at 1 airy in the Leica TCS SP5 II confocal microscope. Images were resolved at 1024×1024 pixels format illuminated with 2%–5% DPSS561 561 nm wave laser using a HyD detector in the BrightR mode and entire Z series were acquired from mouse brain sections. Equivalent stereological regions were acquired for all tissue sections within a given slide. Image series were deconvolved using the Hyugens Professional using the Classic Maximum Likelihood Estimation (CMLE) algorithm together with a determined theoretical PSF established using a routine-based implementation for the Hyugens software. Reconstruction and generation of 3D volumes of deconvolved images were performed using the ImageJ 3D viewer plugin and cell counts were performed blinded on integral 3D volume-rendered images. Sholl analyses were performed using an ImageJ Sholl plugin (Ferreira et al., 2014).

All immunostaining in sets of slides were performed together, using the same batch of primary and secondary antibodies, and blocking and washing solutions. Furthermore, images from different sections within a given slide were acquired on the same day,

always by the same operator and with identical microscope parameters (e.g., same power for the confocal Argon laser; same laser-line potency; same objective; same fluorescence exposure times and offset for a given fluorophore; same camera binning, zoom and ROI magnification; same pinhole aperture; same pixel size; same line averaging; same TCS scanner mode and speed; same z stack step size and optical sectioning).

NeuN quantification
Number of NeuN$^+$ neurons were manually scored from stereological identical images (3D volume-rendered) of the CA1 region of the hippocampus of stained sections (6 images per hippocampal section; 6 hippocampal sections per animal).

Quantification of amyloid deposits
Briefly, M3.2, BAM-10 or 6E10 immunostained sections covering layers II/III and IV of the neocortex or CA1 region of the hippocampus (4 images per section; 6 sections (BAM-10 and 6E10) or 10 sections (M3.2) per animal) were imaged, converted into 8-bit gray scale, 3D volume-rendered and thresholded to highlight immunostained amyloid deposits. Using FIJI software, the percent of immunostained area was calculated for each field and each section.

APP quantification
Briefly, APP immunostained sections covering layers II/III and IV of the neocortex (4 images per section; 6 sections per animal) were imaged, converted into 16-bit gray scale, and thresholded to highlight immunostained APP amounts. Using FIJI software, the percent of immunostained area was calculated for each field and each section.

Methoxy-X04 quantification
Briefly, stained sections covering layers II/III and IV of the neocortex (5 images per section; 4 sections per animal) were imaged, converted into 16-bit gray scale, and thresholded to highlight stained. Using FIJI software, the percent of stained area was calculated for each field and each section.

Quantification of synapses
Images from stereological identical hippocampal CA1 regions from each experimental group (3 images per hippocampi; 4 hippocampal sections per animal) were acquired using a Leica HC PL APO CS 40x /1.10 CORR water objective at 1024 × 1024 pixels resolution with 8-bit bidirectional non-sequential scanner mode at 400 Hz and pinhole at 1 airy in the Leica TCS SP5 II confocal microscope. Z stacks were converted to maximum projection images using LAS AF routine and the LAS AF colocalization plugin processed each projection using subtracted background (25%–36% offset for both channels) and thresholded foreground (35%–45% offset for vGlut-1 channel; 30%–40% offset for PSD-95 channel). Values corresponding to the positive area of vGlut-1/PSD-95 colocalization puncta (synapses) and values for the overall image area for each image was extracted using the LAS AF colocalization plugin and statistically evaluated in GraphPad Prism.

TUNEL assay
Slides were defrosted at room temperature for at least 1 h. After that, sections were hydrated in PBS and fixed with 4% PFA for 10 min. After washes with PBS, sections were blocked (10% NGS; 0,1% BSA and 1% Triton X-100) for 1 h and then equilibrated in TdT buffer (30 mM Tris-HCl; 140 mM Sodium Cacodylate; 1 mM Cobalt chloride; pH 7.2) for 10 min at room temperature. To perform the TUNEL reaction was performed using 1.6 μL of TUNEL Enzyme (11767305001; Roche); 1.2 μL of Biotin-16-dUTP (11093070910; Roche) and 1.2 μL of 1 mM dATP in 200 μL of TdT buffer. The reaction was performed at 37°C for 90 min. The reaction was stopped by incubation with 2x SSC buffer for 10 min. After washes with PBS, Cy3-conjugated Streptavidin (1:200 in blocking solution) and DAPI (2 ug/ml) were incubated for 1 h at room temperature. After PBS washes, sections were mounted with fluoroshield (Sigma-Aldrich). The number of TUNEL$^+$ cells was manually scored from stereological identical images of the CA1 region of the hippocampus of stained sections (4 images per hippocampal section; 8 hippocampal sections per animal).

Quantification of Iba1 colocalization with amyloid deposits
Images from stereological identical neocortical or hippocampal CA1 regions from each experimental group (4 images per section; 6 sections per animal) were acquired using a Leica HC PL APO CS 40x /1.10 CORR water objective at 1024 × 1024 pixels resolution with 8-bit bidirectional scanner mode at 200 Hz in the Leica TCS SP5 II confocal microscope. Z stacks were converted to maximum projection images using LAS AF routine and the LAS AF colocalization plugin processed each projection using subtracted background (45%–55% offset for both channels) and thresholded foreground (65% offset for BAM-10/M3.2 channel; 20%–35% offset for Iba1 channel). Values corresponding to the positive area of colocalization puncta and values for the overall image area for each image were extracted using the LAS AF colocalization plugin and statistically evaluated in GraphPad Prism.

Immunofluorescence on cultured microglia
Microglial cultures were cultivated in glass coverslips. Coverslips were fixed with 4% PFA, washed three times for 5 min in PBS, permeabilized with 0.1% Triton X-100 for 10 min, washed again and incubated for 1 h in blocking solution (5% BSA). Primary antibodies

were added in blocking solution and coverslips were maintained in a humidified chamber for 1 h. Coverslips were washed three times for 10 min with PBS and incubated with secondary antibodies for 1 h in blocking solution. Next, coverslips were washed three times for 10 min with PBS. After the last secondary antibody (when double-labeling was performed), the coverslips were incubated for 1 min with 1 mg/ml DAPI, and rinsed twice in PBS. Coverslips were mounted with Immumount, visualized in a Leica DMI6000B inverted epifluorescence microscope using PlanApo 63X/1.3NA glycerol immersion objective. Images were acquired with 4 × 4 binning using a digital CMOS camera (ORCA-Flash4.0 V2, Hamamatsu Photonics).

For quantification, images were exported as raw 16-bit tiff using the LAS AF software. Background was subtracted in FIJI using the roller-ball ramp in between 35%–50% pixel radius. Images were segmented in FIJI using the local Otsu threshold. Thresholded images were converted to binary mask using the dark background function. Binary mask images were multiplied for their respective original channel images using the image calculator plug-in to generate a masked 32-bit float images relative to each channel. Original coordinate vectors were retrieved from the ROI manager and FIJI returned the mean fluorescent intensity in gray values contained within any single microglia using the multi-measure function. Mean fluorescent intensity for each single microglia were exported and statistically evaluated with the GraphPad Prism software.

Time-lapse video microscopy and FRET assays

For live cell imaging, microglia were plated on plastic-bottom culture dishes (μ-Dish 35 mm, iBidi). Imaging was performed using a Leica DMI6000B inverted microscope. The excitation light source was a mercury metal halide bulb integrated with an EL6000 light attenuator. High-speed low vibration external filter wheels (equipped with CFP/YFP excitation and emission filters) were mounted on the microscope (Fast Filter Wheels, Leica Microsystems). A 440-520nm dichroic mirror (CG1, Leica Microsystems) and a PlanApo 63X 1.3NA glycerol immersion objective were used for CFP and FRET images. Images were acquired with 2x2 binning using a digital CMOS camera (ORCA-Flash4.0 V2, Hamamatsu Photonics). Shading illumination was online-corrected for CFP and FRET channels using a shading correction routine implemented for the LAS AF software. At each time-point, CFP and FRET images were sequentially acquired using different filter combination (CFP excitation plus CFP emission (CFP channel), and CFP excitation plus YFP emission (FRET channel), respectively).

Quantification of biosensors was performed as before (Portugal et al., 2017; Socodato et al., 2015a, 2015b, 2018). In brief, images were exported as 16-bit tiff files and processed in FIJI software. Background was dynamically subtracted from all frames from both channels. Segmentation was achieved on a pixel-by-pixel basis using a modification of the Phansalkar algorithm. After background subtraction and thresholding, binary masks were generated for the CFP and FRET images. Original CFP and FRET images were masked, registered and bleach-corrected. Ratiometric images (CFP/FRET for KRas Src YPet probe and FLIPE glutamate release probe or FRET/CFP for Raichu-Rhoa and Flare.Rhoc sensors) were generated as 32-bit float-point tiff images. Values corresponding to the mean gray values were generated using the multi calculation function in FIJI and exported as mentioned above. KRas Src and glutamate (pDisplay FLIPE-600n^{SURFACE}) biosensors have been previously used in microglia giving reliable FRET to donor signals within the probe dynamic range (Socodato et al., 2015a, 2015b, 2018; Portugal et al., 2017).

For quantification of microglial protrusion velocity, HMC3 microglia expressing Lifeact-mCherry were incubated in DMEM without phenol red plus 15 mM HEPES and recorded (5 min frames for 90 min at 37°C) using appropriate dichroics for red fluorescent protein. Time-lapse images were exported as 16-bit tiff files and processed in FIJI software using the multi kymograph plugin. Protrusion velocities from Lifeact kymograms were extracted using a routine macro from the multi kymograph package in ImageJ.

Preparation of lysates (tissue and cell cultures)

For ELISA, brains were removed, different brains areas were isolated, fast frozen on dry ice and stored at −80°C. Cortices were defrosted and 400 ul of homogenization buffer (50 mM Tris-Base, 4 mM EDTA, 150 mM NaCl, 0.1% Triton X-100 and protease inhibitor cocktail containing AEBSF (Sigma – P8340)). Samples were sonicated (10 pulses of 1 s at 60Hz) and centrifuged for 15 min at 2271 g at 4°C. The pellets were discarded and samples were centrifuged again at 13500 g for 5 minutes at 4°C. The supernatant was used for ELISA and the total amount of protein were estimated using the Pierce BCA protein assay kit.

For all other applications, cell cultures or mice tissues were lysed using RIPA-DTT buffer (150 mM NaCl, 50 mM Tris, 5 mM EGTA, 1% Triton X-100, 0.5% DOC, 0.1% SDS) supplemented with complete-mini protease inhibitor cocktail tablets, 1 mM DTT and phosphatase inhibitor cocktail. Samples were sonicated (6 pulses of 1 s at 60Hz) and centrifuged at 16,000 g, 4°C for 10 min. The supernatants were collected and the protein concentration was determined by the Pierce BCA protein assay kit. All samples were denatured with sample buffer (0.5 M Tris-HCl pH 6.8, 30% glycerol, 10% SDS, 0.6 M DTT, 0.02% bromophenol blue) at 95°C for 5 min and stored at −20°C until use.

Enzyme-linked immunosorbent assay (ELISA)

The concentration of Tnf, $A\beta_{1-40}$ and $A\beta_{1-42}$ were quantified by ELISA following the instructions provided by the manufacturer (Peprotech, UK). Absorbance at 405 nm, with wavelength correction at 650 nm, was measured with a multimode microplate reader (Synergy HT, Biotek, USA). Values corresponding to pg/ml were obtaining by extrapolating a standard concentration curve using recombinant Tnf.

Glutamate determination by fluorimetry

Extracellular glutamate was measured in microglia culture supernatant by the formation of NADH in a reaction catalyzed by glutamate dehydrogenase essentially as elsewhere (Socodato et al., 2015b). Briefly, Tris–acetate (75 mM, pH 8.4) plus NAD and ADP were added to culture supernatants and initial fluorescence arbitrary unit (FAU_i) was quantified in a Luminometer. Glutamate dehydrogenase was added for 30 min to promote the formation of alpha-ketoglutarate and NADH. NADH fluorescence was also determined (FAU_f). Relative extracellular glutamate content was plotted as FAU_f - FAU_i.

Nuclear and cytosolic fractionation

Cultures were washed twice with PBS, and cells were scraped off culture dishes with lysis buffer [50 mM tris-HCl, 5 mM EDTA, 100 mM NaCl, 1 mM DTT, 100 mM phenylmethylsulfonyl fluoride, 200 mM Na_3VO_4, 1% Triton X-100, leupeptin (4 mg/ml)]. Lysates were centrifuged (16,000 g for 10 min at 4°C), the supernatant (cytosolic fraction) was collected, and the pellet (nuclear fraction) was resuspended. All samples were denatured with sample buffer for 5 min at 95°C and stored at −20°C. Both fractions were subjected to SDS–polyacrylamide gel electrophoresis (SDS-PAGE). To confirm the efficacy of the separation assay, we used LAMP-1 (Enzo Life Sciences) as a cytosolic fraction marker and histone H3 (Millipore) as a nuclear fraction marker.

Western blotting

Samples were separated in SDS-PAGE, transferred to PVDF membranes, which were incubated overnight with primary antibodies. Membranes were washed in TBS-T buffer pH 7.6, incubated with peroxidase-conjugated secondary antibodies and developed using an ECL chemiluminescence kit or an ECF fluorescence kit. Images were acquired in a Typhoon FLA 9000 system or ChemiDoc XRS System (Bio-Rad) and quantified by FIJI software.

Electrophysiology

For electrophysiological recordings, acute hippocampal slices from P65-80 male control and Rhoa mutants mice were prepared. All procedures were carried out according to the European Union Guidelines for Animal Care (European Union Council Directive 2010/63/EU) and Portuguese law (DL 113/2013) with the approval of the Institutional Animal Care and Use Committee.

Animals were sacrificed by decapitation after cervical displacement and the brain was rapidly removed in order to isolate the hippocampus. Hippocampi were dissected in ice-cold artificial cerebrospinal fluid (aCSF) containing: 124 mM NaCl, 3 mM KCl, 1.2 mM NaH_2PO_4, 25 mM $NaHCO_3$, 2 mM $CaCl_2$, 1 mM $MgSO_4$ and 10 mM glucose), which was continuously gassed with 95%O_2/5% CO_2. Hippocampal slices were quickly cut perpendicularly to the long axis of the hippocampus (400 μm thick) with a McIlwain tissue chopper and allowed to recover functionally and energetically for at least 1 h in a resting chamber filled with continuously oxygenated aCSF, at room temperature (22–25°C), before being set up for electrophysiological recordings.

For extracellular recordings of field Excitatory Post-Synaptic Potentials (fEPSP), slices were transferred to a recording chamber for submerged slices (1 mL capacity plus 5 mL dead volume) and were constantly superfused at a flow rate of 3 ml/min with aCSF kept at 32°C, gassed with 95% O_2 – 5%CO_2. Evoked fEPSP were recorded extracellularly using a microelectrode (4 to 8 M extracellularly using feraCSF solution placed in the *stratum radiatum* of the CA1 area). fEPSP data were acquired using an Axoclamp-2B amplifier (Axon Instrumnets, USA). fEPSPs were evoked by stimulation through a concentric electrode to the Schaffer collateral fibers. Each individual stimulus consisted of a 0.1 ms rectangular pulse applied once every 20 s, except otherwise indicated. Averages of six consecutive responses were continuously acquired, digitized with the WinLTP program (Anderson and Collingridge, 2001) and quantified as the slope of the initial phase of the averaged fEPSPs. The stimulus intensity was adjusted at the beginning of the experiment to obtain a fEPSP slope close to 1 mV/ms, which corresponded to about 50% of the maximal fEPSP slope.

θ-burst stimulation was used to induce LTP because this pattern of stimulation is considered closer to what physiologically occurs in the hippocampus during episodes of learning and memory in living animals (Albensi et al., 2007). After obtaining a stable recording of the fEPSP slope, a θ-burst of stimuli, consisting of 1 train of 4 bursts (200 ms interburst interval), each burst being composed of 4 pulses delivered at 100 Hz [1 x (4 × 4)], was applied, and the stimulus paradigm was then resumed to pre-burst conditions up to the end of the recording period (60 min after burst stimulation). LTP magnitude was quantified as % change in the average slope of the fEPSP taken from 50-60 min after LTP induction as compared with the average slope of the fEPSP measured during the 10 min before induction of LTP. fEPSPs were recorded under basal stimulation conditions (standard stimulus intensity and frequency) and stability of fEPSP slope values guaranteed for more than 10 min before changing any protocol parameter. One or two slices per animal were tested at each experimental day.

Behavioral tests

Testing procedures were conducted in the dark phase of the light/dark cycle. Only male mice were used in behavioral analysis. Before each session, mice were removed from their home cage in the colony room and brought into the adjacent testing rooms (illuminated with 100 lux and attenuated noise). Behavioral tests were performed in 3 consecutive days in the following order: (1) elevated plus-maze; (2) open field; (3) novel object recognition. All tests were video-recorded. In the elevated plus-maze and open-field tests movement and location of mice were analyzed by an automated tracking system equipped with an infrared-sensitive camera (Smart Video

Tracking Software v 2.5, Panlab, Harvard Apparatus). Data from the object recognition test were analyzed using the Observer 5 software (Noldus Information Technology, Wageningen, the Netherlands). All apparatus were thoroughly cleaned with neutral soap after each test session.

Elevated plus-maze (EPM)
The maze was made of opaque gray PVC consisting of four arms arranged in a plus-shaped format; two arms have surrounding walls (closed arms, 37x6 cm x18 cm-high), while the two opposing arms have no walls (open arms, 37x6 cm). The apparatus is elevated by 50 cm above the ground. Mice were placed on the central platform facing an open arm and were allowed to explore the maze for 5 min. Open arms entries and time spent in open arms were obtained automatically (video tracking) and used to assess anxiety-like behavior.

Open field (OF)
Mice were placed in the center of an OF apparatus (40 × 40 × 40 cm) and then allowed to move freely for 10 min. The distance traveled, peripheral activity and center activity (locomotion in the central section of the OF) were obtained automatically (video tracking).

Novel object recognition (NOR)
The NOR test was performed as previously described (Leger et al., 2013). Briefly, the test apparatus consists of an open box and the objects used are made of plastic, glass or metal in three different shapes: cubes, pyramids and cylinders. The test consists of three phases. During habituation phase mice are allowed to explore the apparatus for 10 min (time used to perform OF test). The following day, the acquisition/sample phase starts by placing each mouse in the apparatus with two identical objects (familiar) for 10 min. Then the mouse goes back to its home cage. After 4 h (inter-trial interval, ITI), the retention/choice session is performed. In this phase, the apparatus contains a novel object and a copy of the previous familiar object; animals are allowed to explore these objects for 3 min. Exploration was defined as follows: mouse touched the object with its nose or the mouse's nose was directed toward the object at a distance shorter than 2 cm (Ennaceur et al., 2005). Circling or sitting on the object was not considered exploratory behavior. Increased time spent exploring the novel object serves as the measure of recognition memory for the familiar object. Positive difference between the exploration time for novel and familiar objects and a discrimination index (DI) above 0.5 were used as indicators of object recognition (Ennaceur et al., 2005). The discrimination index (DI) was calculated as index of memory function, DI = (time exploring the novel object) / (total time spent exploring both objects) (Ennaceur et al., 2005).

Cloning of shRNAs into pSicoR-GFP vector
The cloning was performed as previous described (Ventura et al., 2004). Briefly, shRNA oligos (Rhoa sense: TGTCAAGC ATTTCTGTCCTTCAAGAGAATTTGGACAGAAATGCTTGACTTTTTTC and antisense: CGAGAAAAAAGTCAAGCATTTCTGTC CAAATTCTCTTGAAATTTGGACAG AAATGCTTGACA; Rhob sense: TCGACGTCATCCTTATGTGCTTTTCAAGAG AAAGCACAT AAGGATGACGTCGTTTTTTTC and antisense: TCGAGAAAAAACGACGT CTTATGTGCTTTCTCTTGAAAAGCACATAAGGATGAC GTCGA; Rhoc sense: TACCTG AGGCAAGATGAGCATATTCAAGAGATATGCTCATCTTGCCTCAGGTTTTTTTC and antisense: GAG AAAAAAACCTGAGGCAAGATGAGCATATCTCTTGAATATGCTCATCT TGCCTCAGGTA were annealed and cloned into HpaI-XhoI-digested pSicoR using the T$_4$ ligase. Oligos insertion into the vector was validated using PCR and confirmed by sequencing. A control shRNA with no mammalian target (directed against DsRed2; referred to as scrambled) was used in experiments using the pSicoR as before (Portugal et al., 2017).

Lentiviruses/Retroviruses production
This protocol was performed exactly as described elsewhere (Socodato et al., 2012; Mejía-García et al., 2013). Low passage HEK293T cells were seeded in 100 mm culture dishes. When cultures reached ∼80% confluence cells were co-transfected overnight with viruses-producing plasmids using jetPRIME®. Transfection ratios were as follows: 6 μg of shRNA plasmids to 3 μg of psPAX2 to 3 μg of VSVG (2:1:1) for lentiviruses production or 8 μg of VSVG (or Src^{Y416F} or Src^{Y527F} construct to 4 μg of pUMVC to 2 μg of VSVG (4:2:1) for retroviruses production. The next day, normal growth media replaced transfection media and cells were cultivated for an additional 48 h. Next, media with viral particles were collected, centrifuged at 906 g for 15 min at 4°C, and the supernatant was collected into new tubes and kept at −80°C.

Total RNA extraction, cDNA synthesis and qRT-PCR
Total cerebral cortex RNA was extracted using the Direct-zol™ RNA MiniPrep kit according to the manufacturer's instructions. RNA from FACS-sorted microglia was harvested using the Quick-RNA MicroPrep kit. RNAs quality and concentration were all determined using a NanoDrop ND-1000 Spectrophotometer. cDNA synthesis was performed using 100-500 ng of total RNA (DNase I treated) with SuperScript® III First-Strand Synthesis SuperMix.

qRT-PCR was carried out using iQ SYBR® Green Supermix on an iQ5 multicolor real-time PCR detection system (Bio-Rad). The efficiency was analyzed using a log-based standard curve. Expression of PCR transcripts between genotypes was calculated using the 2$^{-deltaCt}$ method with *Yhwaz* serving as the internal control gene.

Preparation of Aβ oligomers

Human Aβ$_{1-42}$ peptide (Genscript) was dissolved to 2 mM in DMSO essentially as before (Silva et al., 2017). For oligomer formation, Aβ$_{1-42}$ peptide was diluted to 100 μM in Ca^{2+}-free HBSS and incubated for 24-48 h at 4°C. Oligomers were used at final concentration of 200 nM in microglial cultures.

Aβ$_{1-42}$ uptake assay

HMC3 microglial cells were seeded on 96-well plate (PerkinElmer) at 1 × 10^4 cells per well using an automated Multidrop dispenser (Thermo Scientific) and incubated for 24 hours at 37°C in 5% CO$_2$. Then, cells were co-transfected with FKBP-YFP and FRB-Lyn and or with Rhoa-YF (CA) and FRB-Lyn. For chemogenetic activation of Rhoa, cells were pre-treated with rapamycin (Sigma; 500 nM) for 15 min. Different non-transfected cultures were also pre-incubated with AZD 0530 (Src inhibitor; 500 nM) or vehicle (DMSO) for 15 min. Afterward, cells were incubated with 10 μg/ml Aβ(1–42) HiLyte^{TM} Fluor 555-labeled (Eurogentec) for 90 min at 37°C in 5% CO$_2$. Cells were then thoroughly washed, fixed with 4% MP-paraformaldehyde (w/v), permeabilized with 0.1% (v/v) Triton X-100 (Sigma) for 30 min at room temperature and labeled with DAPI and HCS CellMask (Invitrogen).

Images of microglial cultures were acquired using IN Cell Analyzer 2000 microscope (GE Healthcare) using a large chip CCD Camera (binning 2X2) and a Nikon 20x/0.45 NA Plan Fluor objective. Images of Aβ$_{1-42}$, DAPI-stained nuclei, HCS CellMask and in some conditions transfected (YFP$^+$) cells were acquired using appropriate dichroics for TexasRed, DAPI, Cy5 and FITC channels, respectively. For Aβ$_{1-42}$ signal quantification, the CellProfiler (3.1.8) software was used. For nuclei segmentation, a global thresholding strategy was used followed by Otsu local thresholding. Clumped microglial nuclei were distinguished and individualized. Afterward, microglial cells were segmented using the raw HCS CellMask image through a propagation algorithm based on the minimum cross entropy thresholding method applied to the HCS CellMask channel using segmented nuclei as start point and then spanning up to the edges of the labeled microglial plasma membrane. The mean fluorescent intensity of Aβ$_{1-42}$ HiLyte^{TM} Fluor 555 in each microglial cell was retrieved and plotted for statistical evaluation.

QUANTIFICATION AND STATISTICAL ANALYSIS

Graphs are displayed as dot plots showing full data dispersion with the mean and the 95% confidence interval of the mean. $p < 0.05$ was the cut-off for considering statistically significant difference between comparisons in sampled groups. Experimental units in biological replicates were evaluated *a priori* for Gaussian distribution using the D'Agostino & Pearson omnibus normality test. When comparing only 2 experimental groups, the unpaired Student t test with equal variance assumption was used for data with normal distribution, while the Mann-Whitney test was used for with non-parametric data. When comparing 3 or more groups, ordinary One-way ANOVA followed by the Bonferroni's multiple comparations test was used for data with normal distribution, and the Kruskal-Wallis test followed by Dunn's multiple comparations test was used for non-parametric data. When comparing 4 groups with 2 independent variables, Two-way ANOVA followed by the Bonferroni's multiple comparations test was used. All imaging quantifications (cell cultures, FACS or mice tissue sections) were blind performed. All statistical analyses were carried out using the Graph Pad Prism 7.0 software. Further statistical details are indicated in the figure legends.